divided by 2 in order to obtain the shaded histogram in Fig. 2(c).

[12]S. R. Amendolia *et al.*, Phys. Lett. 44B, 119 (1973); G. Charlton *et al.*, Phys. Rev. Lett. 29, 515 (1972).
[13]J. W. Chapman *et al.*, Phys. Rev. Lett. 29, 1686 (1972).
[14]H. Bøggild *et al.*, Nucl. Phys. B27, 285 (1971).
[15]G. G. Beznogikh *et al.*, Phys. Lett. 43B, 85 (1973).
[16]M. Holder *et al.*, Phys. Lett. 35B, 361 (1971).
[17]V. V. Ammozov *et al.*, Phys. Lett. 42B, 519 (1972).
[18]W. R. Frazer *et al.*, Phys. Rev. D 7, 2647 (1973).
[19]U. Amaldi *et al.*, Phys. Lett. 36B, 504 (1971).
[20]G. G. Beznogikh, Phys. Lett. 30B, 274 (1969).
[21]V. Bartenev *et al.*, Phys. Rev. Lett. 29, 1755 (1972).
[22]U. Amaldi *et al.*, Phys. Lett. 43B, 231 (1973).
[23]Both Monte Carlo–generated events for particular reactions as well as the real data, where it is possible to check this, indicate that there is little difference, generally less than 0.5 units, between η and the real longitudinal rapidity $y = \frac{1}{2}\ln[(E+p_{\parallel})/(E-p_{\parallel})]$.
[24]The different shapes of the data near $\eta = 0$ and near $\eta = -6$ result from the use of the pseudorapidity and the angle errors on the fast forward tracks.

PHYSICAL REVIEW D VOLUME 9, NUMBER 5 1 MARCH 1974

Systematic study of $\pi^{\pm}p$, $K^{\pm}p$, pp, and $\bar{p}p$ forward elastic scattering from 3 to 6 GeV/c*

I. Ambats, D. S. Ayres, R. Diebold, A. F. Greene,† S. L. Kramer, A. Lesnik,‡ D. R. Rust,§ C. E. W. Ward, A. B. Wicklund, and D. D. Yovanovitch†
Argonne National Laboratory, Argonne, Illinois 60439
(Received 9 August 1973)

Measurements of $\pi^{\pm}p$, $K^{\pm}p$, pp, and $\bar{p}p$ elastic scattering are presented for incident momenta of 3, 3.65, 5, and 6 GeV/c and momentum transfers typically 0.03 to 1.8 GeV^2. The angle and momentum of the scattered particle were measured with the Argonne Effective Mass Spectrometer for 300 000 events, yielding 930 cross-section values with an uncertainty in absolute normalization of ±4%. Only the K^+ and proton data show any significant change in slope of the forward diffraction peak with incident momentum. The particle-antiparticle crossover positions are consistent with no energy dependence, average values being 0.14 ± 0.03, 0.190 ± 0.006, and 0.162 ± 0.004 GeV^2 for π's, K's, and protons, respectively; these errors reflect both statistics and the ±1.5% uncertainty in particle-antiparticle relative normalization. Differences between particle and antiparticle cross sections isolate interference terms between amplitudes of opposite C parity in the t channel; these differences indicate that the imaginary part of the odd-C nonflip-helicity amplitude has a $J_0(r(-t)^{1/2})$ structure for $-t < 0.8$ GeV^2, as predicted by strong absorption models. The cross-section differences for $K^{\pm}$ and proton-antiproton are in qualitative agreement with the predictions of ω universality, the agreement improving with increasing energy. The corresponding quark-model predictions relating the $\pi^{\pm}$ and $K^{\pm}$ differences failed by more than a factor of 2. We have combined our $\pi^{\pm}$ cross sections with other data to better determine the πN amplitudes in a model-independent way; results of this analysis are presented.

I. INTRODUCTION

Elastic scattering of elementary particles is a most fundamental process. At high energies such scattering is dominated by diffraction and is related to the inelastic processes through unitarity; in t-channel language this is usually described as Pomeron exchange. At intermediate energies, quantum-number-exchange amplitudes are also present and are often parameterized in terms of Regge-pole exchange.

Some of these latter amplitudes can be obtained by a careful comparison of similar reactions related by simple, well-defined symmetries. For example, the difference between particle and antiparticle elastic scattering from protons results from a sign change in the interference between even and odd C-parity exchanges in the t channel. Near the forward direction the dominant even-C amplitude is the imaginary helicity-nonflip amplitude, and the interference between it and the odd-C amplitude can be used to study the imaginary nonflip part of the odd-C exchange amplitude. This amplitude is often taken to be ρ exchange in the case of πp scattering and ω exchange for Kp and pp scattering.

The experimental particle-antiparticle differences can be compared with the expectations of various models. Such a comparison was made by Davier and Harari[1] for $K^{\pm}p$ scattering at 5 GeV/c; they found the amplitude to be consistent with the $J_0(r(-t)^{1/2})$ structure predicted by the dual absorption model. In the case of $\pi^{\pm}p$ scattering, detailed amplitude analyses have been made[2–5]; the pion

cross-section difference is important not only for the imaginary nonflip $I=1$ exchange amplitude, but is also involved in the calculation of other small amplitudes.

To understand the details of elastic scattering, one needs a systematic study of as many reactions as possible, as a function of both energy and momentum transfer. Until now, no such study has been made in our energy region, 3 to 6 GeV/c incident momentum. The results of many experiments have been reported in this energy range (see, for example, Refs. 6–21), but most of these have been studies of one reaction at one or two energies. Uncertainties in relative normalization made it difficult to reliably determine the particle-antiparticle differences.[22]

In the experiment reported here a total of 300 000 events was used to determine elastic scattering cross sections for π^+p, π^-p, K^+p, K^-p, pp, and $\bar{p}p$ at four incident momenta, 3, 3.65, 5, and 6 GeV/c. The t range varied slightly with energy and particle type, but was typically 0.03 to 1.8 GeV^2. The angle and momentum of the scattered particle were measured with the Argonne Effective Mass Spectrometer using magnetostrictive readout spark chambers.[23] Although the over-all uncertainty in absolute normalization is ±4%, special attention was given to the particle-antiparticle relative normalization and an uncertainty of ±1.5% was achieved. A summary of some of the more interesting results has been reported previously.[24]

The experimental method is outlined in Sec. II, and the data reduction and systematic uncertainties are discussed in Sec. III. The results and comparisons with previous experiments and models are presented in Sec. IV. A πN amplitude analysis is described in Sec. V, and conclusions are summarized in Sec. VI.

II. EXPERIMENTAL METHOD

A. Beam

The experiment was performed at the Zero Gradient Synchrotron (ZGS) with the Argonne Effective Mass Spectrometer.[23] The unseparated incident beam had a maximum momentum of 6 GeV/c and a momentum spread of ±1.5%. A six-counter hodoscope at the first focus tagged the individual particle momenta to ±0.2%. The beam spot at the 20-in.-long, 2-in.-diameter liquid hydrogen target was typically 0.75 in. in diameter, achromatic in position and angle. Variable horizontal and vertical collimators near the copper production target were used to adjust the beam flux by reducing the beam solid angle from its maximum of ±7 mrad horizontally by ±17 mrad vertically. The beam had a maximum divergence at the hydrogen target of ±8 mrad horizontally and vertically, but the trajectories of incident particles for events of interest were measured to better than ±1 mrad by spark chambers upstream of the hydrogen target.

Four ethylene-gas threshold Čerenkov counters provided tagging information to label incident beam particles as pions, kaons, or protons. Ambiguities in identification were minimized by separating with a 16° bend the two counters which were set to detect only pions, and by similarly separating the two counters which were set above kaon threshold. These last two counters detected both pions and kaons. The counter efficiencies were all greater than 99.9%. Six beam-defining anticoincidence counters along the beam line considerably reduced both the beam halo and nonsense Čerenkov-counter signatures. Beam composition varied with momentum, but typical $\pi/K/p$ ratios were 99/1/0.1 for negatives and 32/1.5/66 for positives. Misidentification of particles labeled as kaons or antiprotons was less than 0.2% for both beam polarities.

The beam Čerenkov counters could not distinguish π's from μ's and e's, and the incident pion flux had to be corrected for the μ-e contamination. This contamination was measured by taking pressure curves with a sensitive threshold Čerenkov counter located downstream of the spectrometer. The μ-e fractions, corrected for pion decays in the spectrometer, are given in Table I.

In order to ensure equality of accidental coincidences and other rate effects, the total incident particle flux was kept constant at about 2×10^5 per 0.7-sec ZGS pulse for both beam polarities. This was accomplished by defocusing the incident proton beam at the production target when running with a positive secondary beam, and by making small adjustments of the beam-defining collimators.

B. Spectrometer

Figure 1 shows a plan view of the spectrometer, the basic component of which was a large dipole magnet, with an aperture 84 in. wide by 26 in. high. The magnet had a central field of 11.4 kG,

TABLE I. Percentage contamination of the pion beam by fast muons and electrons. Within errors, $\mu^-/\pi^- = \mu^+/\pi^+$ and $e^-/\pi^- = 2e^+/\pi^+$.

p (GeV/c)	μ^+/π^+	e^+/π^+
3	1.8	1.6
3.65	1.7	1.1
5	1.2	0.6
6	0.9	0.2

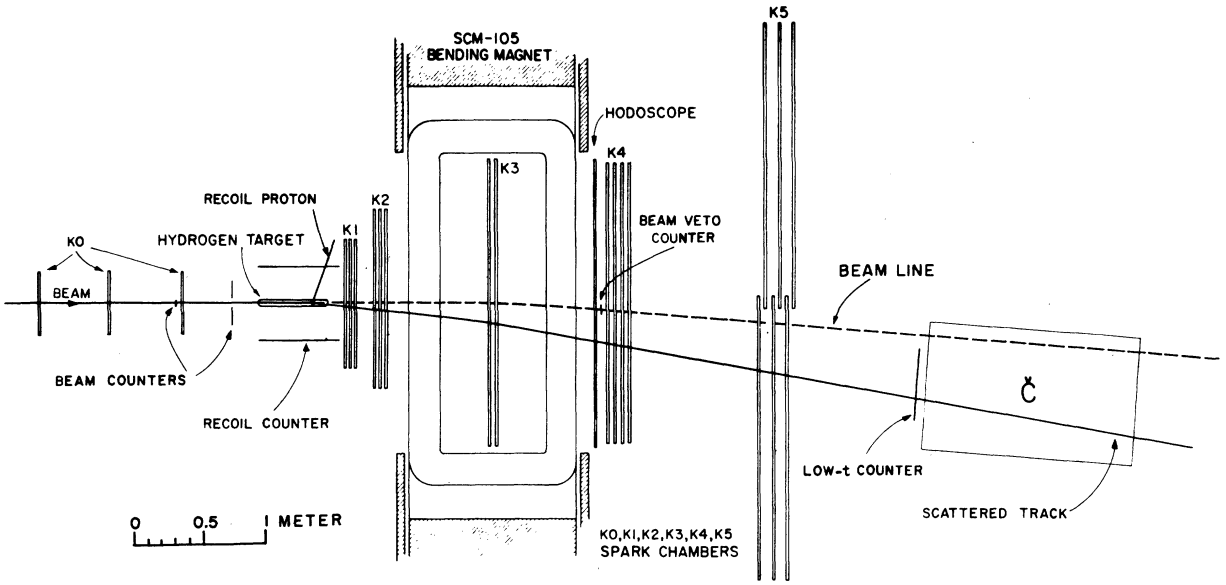

FIG. 1. Sketch of the Argonne Effective Mass Spectrometer as used to study elastic scattering.

an effective length of 40 in., and an $\int \vec{B} \cdot d\vec{l}$ which was constant to about 20% over the aperture. The vertical and horizontal components of the field were measured over an 84 000-point grid,[25] and the fitted results, as described by a 2800-parameter field-generating computer program, were accurate to 0.1% of the central value.

Spark chamber sets $K1$ through $K5$ measured the trajectories of secondary particles produced in the hydrogen target. The readout of the wire chambers was provided by 40 magnetostrictive lines with electronics which could record up to four sparks per readout. Each chamber was constructed from two foils 0.375 in. apart, each consisting of 4-mil-diameter aluminum wires flattened to 1 mil and epoxied to 3-mil Mylar sheets with 0.5-mil aluminum foil backing. Wire spacing varied from 20 per inch ($K0, K4$) to 40 per inch ($K1, K2, K3$), with a total of 60 000 wires. The density of a typical chamber was 0.07 g/cm^2 (0.002 radiation lengths). The $K5$ chambers were the largest constructed by this method and had active areas 79 in. wide by 46 in. high. The six $K5$ chambers were divided into two overlapping sets of three so their total area matched the spectrometer acceptance. The acceptance was ±400 mrad horizontally by ±140 mrad vertically, nearly independent of momentum for the fast tracks from elastic scattering.

Each of the $K0$, $K4$, and $K5$ chambers had two planes of orthogonal wires, giving horizontal and vertical spark coordinates directly. The $K1$ and $K2$ chambers each had a plane of vertical wires and a plane of wires at ±30° to the vertical. These provided horizontal and vertical coordinates and were used to resolve ambiguities in multiple-track events. The $K3$ chamber inside the magnet had only vertical wires which were extended out the gap of the magnet for readout in a low field region. These provided only horizontal position information. The readout lines of all chambers close to the magnet were protected from the fringe field by iron shields, 0.75 to 2 in. thick. By careful surveying of chamber positions and by altering the ends of the magnetostrictive lines used for readout, it was possible to measure and correct for such effects as the different formation times of spark and fiducial currents, the displacement of effective spark formation planes from the center of the chambers, and $\vec{E} \times \vec{B}$ effects in the $K3$ chambers. The spatial resolution of the chambers was about ±0.5 mm. Combined with the effects of multiple scattering, this yields the over-all resolutions for elastic scattering shown in Table II.

A gas mixture of 89% neon, 10% helium, and 1%

TABLE II. Resolution of the spectrometer for the outgoing horizontal (σ_θ) and vertical (σ_ϕ) angles at the hydrogen target, outgoing track momentum (σ_p), and missing-mass squared ($\sigma_{M_x^2}$) for elastic scattering. Errors in θ and p are highly correlated.

Momentum (GeV/c)	σ_θ (mrad)	σ_ϕ (mrad)	σ_p (MeV/c)	$\sigma_{M_x^2}$ (GeV^2)
3	0.8	0.8	27	0.053
3.65	0.8	0.7	35	0.067
5	0.7	0.6	54	0.103
6	0.7	0.6	70	0.133

ethanol was circulated through the chambers and through a purifier at about 30 ft^3 per hour. The ethanol concentration was maintained by bubbling the gas through liquid alcohol at −5 °C and 2 psig and monitored with a gas chromatograph which was also sensitive to air contamination of a few ppm. With this mixture and an 80-V dc clearing field, the chambers had a sensitive time of about 1 μsec. High-voltage pulses of 7 kV amplitude and 60 nsec full width at half maximum were applied by thyratrons, which discharged storage capacitors across the chambers about 400 nsec after an event of interest occurred. The chambers were resistively terminated to improve their multiple-track efficiency. The high-voltage pulse was followed by a pulsed clearing field of 200 V and 6-msec duration. The resulting recovery time was less than 10 msec. The chamber operating parameters were optimized in the laboratory[26] to achieve three-track efficiencies of 92–96%, yielding single-track efficiencies of about 98% for this experiment.

C. Trigger scheme

The spectrometer was triggered by a beam particle in coincidence with one of two proton recoil scintillation counters and with one or more counts in the appropriate half of the 40-counter hodoscope at the spectrometer magnet exit. The hodoscope counters were made of 0.125-in. thick scintillator. Inelastic events were suppressed by two 28-in.-wide by 30-in.-long veto counters, which covered the central part of the magnet pole faces. Triggers from noninteracting beam particles were reduced by a 3-in.-square beam veto counter at the magnet exit. The two recoil counters, 23 in. long by 12 in. high, were placed in vertical planes 10.4 in. from the hydrogen-target center line. They subtended a 60° azimuth for recoil protons and were separated from the liquid hydrogen by only an air path and 20 mils of Mylar.

In order to extend the measurements to $-t \leq 0.04$ GeV^2 and to monitor the efficiency of the recoil counters, a single "low-t" counter downstream from the spectrometer was used to trigger on small-angle scatters from 30 to 110 mrad. This counter was followed by a threshold Čerenkov counter which was used in the kaon trigger to veto "low-t" candidates produced by $K_{\mu 2}$ decays of beam kaons. For each incident particle type, data from all three types of triggers were recorded simultaneously:

(1) beam · left recoil · right hodoscope · $\overline{\text{vetoes}}$,
(2) beam · right recoil · left hodoscope · $\overline{\text{vetoes}}$,
(3) beam · low t · $\overline{\text{vetoes}}$.

Furthermore, data were accumulated simultaneously for incident pions, kaons, and protons (or antiprotons) for each beam polarity, with triggers from pions and protons electronically suppressed relative to those from kaons and antiprotons. In order to make the spectrometer look the same to incident particles and antiparticles, the polarity of the spectrometer magnet was reversed several times. To further reduce the effects of possible time-dependent systematic errors which might affect the particle-antiparticle cross-section differences, reversals of the magnet were alternated with reversals of beam polarity.

D. Data collection and on-line analysis

The spectrometer was on line to an EMR-6050 computer whose primary function was to collect the data from up to 45 triggers per ZGS pulse and to store the results on magnetic tape during the 3.5 seconds between beam bursts. The raw data were supplied to the computer through a Science Accessories Corporation MIDAS electronics system. The data consisted of (1) the contents of four scalers for each of the 40 spark-chamber readouts, with a least count of 10 mils; (2) tag bits indicating which scintillation counters had fired for each event, including the 40 trigger hodoscope counters, the momentum hodoscope, veto counters in the magnet, the two recoil counters, and the "low-t" counter; (3) the type of the trigger coincidence responsible for each event; (4) pulse heights from the beam Čerenkov counters; (5) contents of the fast logic scalers which accumulated normalization information; (6) the reading of a digital voltmeter which cycled through the secondary beam magnet shunt voltages; and (7) a bit indicating the passage of an extra beam track through the apparatus in the time between the interaction and the spark-chamber firing.

The computer had 32 000 words of 24-bit memory, 1.9 μsec cycle time, floating-point hardware, priority interrupts, an oscilloscope display, two fast tape drives, and other peripherals. In the time between beam pulses, it completely analyzed 30% of the events, monitored spark-chamber efficiencies and scintillation-counter rates, checked magnet currents, provided an oscilloscope display of the geometrical reconstruction of events and histograms of results, and warned the experimenters of possible spark-chamber malfunctions. The powerful diagnostic tool provided by the on-line computer system[27] allowed the experiment to be tuned and debugged quickly, helped to maintain a consistently high level of hardware performance during the data taking, and made feasible the on-line study of possible systematic effects.

III. DATA REDUCTION

A. Event selection and inelastic background

Although the recoil proton was part of the triggering scheme, the recoil direction and momentum were not measured. To separate elastic events from the inelastic background, the scattered particle was assumed to have the same mass as the beam particle, and the missing mass squared, M_x^2, was calculated. Typical distributions are shown in Fig. 2. The peak at M_p^2 corresponding to elastic scattering has very little background. The rms widths of the peaks (Table II) were found to range from 0.05 GeV^2 at 3 GeV/c to 0.13 GeV^2 at 6 GeV/c. This is to be compared with the 0.27-GeV^2 separation between M_p^2 and the beginning of pion-nucleon phase space. Cuts were made on M_x^2 centered at 0.78 GeV^2 with half-widths of 0.37, 0.40, 0.50, and 0.56 GeV^2 for beam momenta of 3, 3.65, and 6 GeV/c, respectively. These cuts were offset from the nominal recoil mass to minimize the amount of background from pion-producing reactions at larger M_x^2.

A small correction was applied to the cross sections to account for inelastic contamination. We assumed that the inelastic background is predominantly due to single-pion production, which populated the high side of the missing-mass distribution starting at $M_x^2 \approx 1.16$ GeV^2. We fitted the region with $M_x^2 > 1.16$ GeV^2 to a phase-space distribution taking into account the spectrometer resolution and extrapolated this fit beneath the elastic peak. The resulting correction was less than 2% in all cases, with an uncertainty $\lesssim \pm 0.5\%$.

The 3-GeV/c π^+ and K^+ missing-mass spectra showed a tail at the 1% level for small M_x^2 not present in the π^- and K^- spectra. We attributed this tail to events with a fast forward proton (u-channel processes) and assumed that this background gave rise to a flat distribution in M_x^2 under the forward elastic peak. An empirical correction of 0.1 mb/GeV^2, independent of t, was made to the 3-GeV/c π^+ data, and a 2% correction was applied to the 3-GeV/c K^+ data. This effect was negligible at higher incident momenta.

B. Geometric acceptance and fiducial cuts

Each recoil counter subtended an azimuth of 60° with an uncertainty of ±1°. The uncertainty is due to the alignment accuracy and possible edge effects. The recoil-proton azimuthal distribution, as calculated from the fast forward particle direction, contained both the desired signal (azimuth within ±30° of the horizontal) and a random ~2% background. The background events were primarily due to elastic scatters accompanied by a δ ray which triggered the recoil counters, and it was

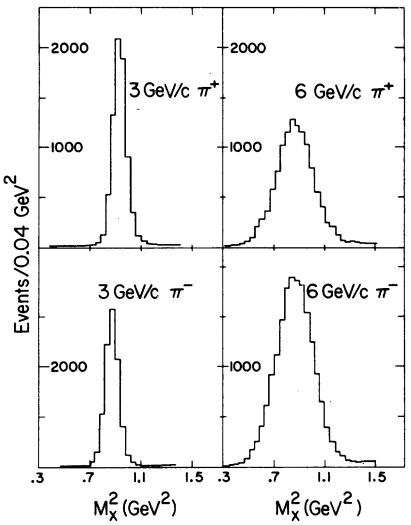

FIG. 2. Missing-mass spectra for $\pi^{\pm}p \to \pi^{\pm}X$ for recoil triggers; the spectra are dominated by the elastic scattering signal at M_p^2.

necessary to reject events in which the proton missed the recoil counters. A cut of ±34° was chosen to allow for multiple scattering and measurement errors.

An additional requirement was that events in the final data sample have a production vertex within the central 15.33 in. of the 20-in.-long liquid hydrogen target. The vertex resolution was sufficient at all momentum transfers to ensure that a correction of no more than a 1% was needed to account for losses caused by measurement errors. This vertex cut was required because (1) the upstream 2 in. of the target was occluded by a $\frac{1}{2}$-in.-thick steel frame which supported the target vacuum window, (2) protons from the downstream 2 in. of the target with recoil angles less than 70° missed the counters altogether, and (3) practically all of the nonhydrogen background came from the target flask windows and was eliminated by this cut.

Cross sections for $-t < 0.04$ GeV^2 were obtained from the "low-t" trigger events, with the same vertex cut as described above. The physical outline of the "low-t" counter could be measured directly from the data, but since the counter subtended an opening angle of only ±28 mrad in the vertical, it was necessary to fold the observed divergence of the incident beam (±6 mrad) into the acceptance calculation. In practice, weights were assigned to the "low-t" events after choosing a minimum cutoff in t which ensured that the weights would vary by less than 10% over the data sample.

Within statistics, the cross sections for recoil and for "low-t" triggers agreed in the overlap

region ($0.04 < -t < 0.15$). Furthermore, the recoil cross sections were independent of magnet polarity and were the same for left and right recoil counters separately. Both the vertex and the azimuthal distributions were quite flat, and making tighter cuts on these quantities did not change the results within statistics. The acceptance corrections have an uncertainty of ±2% from possible geometrical biases and non-Gaussian losses from the fiducial cuts.

The efficiency of the recoil trigger was monitored as a function of t by looking at events having a "low-t" trigger and a proton trajectory calculated to hit a recoil counter. As expected, this efficiency depended only on t and not on the beam energy or on the nature of the incident particle. Recoil protons with momenta less than 200 MeV/c tended to stop inside the target and for this reason we did not use the recoil cross section for $-t < 0.04$ GeV^2. The average efficiency was 84% for $-t$ between 0.04 and 0.05 GeV^2, 97% for $-t$ between 0.05 and 0.06 GeV^2, and 99% for $-t$ greater than 0.1 GeV^2.

C. Miscellaneous corrections

About 20% of the raw triggers were rejected immediately for one of the following reasons: (1) The beam momentum hodoscope pattern was ambiguous; (2) the passage of a beam particle was detected after the event that triggered the spark chambers had occurred; (3) no beam tracks were found in the beam chambers within a 15-mrad angular cut; or (4) more than one beam track was reconstructed. The measured incident flux for each reaction was corrected for these random losses.

Periodically the spectrometer was triggered on beam tracks with the target empty, allowing us to reconstruct the momentum and angular distribution of the incident beam. In particular, this information was used to check that criterion (3) above was unbiased, by comparing the distribution of incident angles for beam triggers with those for elastic scatters; the 15-mrad cut corresponded to the same fraction of events lost in both samples (0.5%). The other beam criteria were also checked for possible biases and none were found.

Using the beam-track triggers we could also estimate losses due to interactions in the spectrometer and due to program inefficiency (i.e., anything which prevented the beam particles from reconstructing with the correct momentum). In particular, because of interactions and decays in the beam line, 0.8% of the incident protons and 2.3% of the pions had too low a momentum. The extra 1.5% contamination in the pion spectrum was attributed to slow muons coming from pion decays upstream of the target. This fraction was nearly independent of incident momentum, presumably because at higher energies, although there were fewer decays, the decay muons were more collimated in the forward direction and had a better chance of getting through the beam anticounters. K^+ decays upstream of the target were calculated to reduce the effective K beam by 2.4% (1.5%) at 3 (6) GeV/c.

A small fraction of the beam-track events failed to reconstruct because of interactions in the spectrometer (2–4%) and spark-chamber inefficiency (~2%). The total material in the spectrometer was 1.4 g/cm^2 equivalent of carbon, and the corresponding interaction losses were checked empirically by looking at failing beam tracks on the computer display scope. Typical corrections were 2% for incident $\pi^\pm$.

At small angles the correction for interaction losses in the liquid hydrogen with the target full was $0.21\% \times \sigma_{\text{tot}}$ (mb). In fact, this correction included double elastic scatters in the hydrogen, some of which were indistinguishable from single scatters and contributed to the measured cross section. The fraction of double scatters which satisfied our fiducial cuts was calculated for each reaction as a function of momentum transfer, and some typical values are shown in Table III. The biggest correction required was 13% ($\bar{p}$ at $-t = 0.5$ GeV^2), and in general the effect was significant only at large momentum transfers, where the statistical uncertainties were also large.

Corrections using the Monte Carlo technique were made for decays in flight of the scattered pions and kaons, and these corrections were checked against the number of pion and kaon beam tracks that failed to reconstruct with the correct momentum. Because of their small decay angles in the laboratory, pions which decayed between the last two spark-chamber sets satisfied the reconstruction criteria. On the other hand, only 3% of the kaons which decayed could reconstruct as elastic scatters. Typical corrections were 0.9% for pions and 9% for kaons at 5 GeV/c. In addition, 2–4% of the scattered kaons decayed

TABLE III. Typical values of the double-scattering correction in percent. The raw cross sections are corrected downward.

$-t$ (GeV^2)	π^+	π^-	K^+	K^-	p	$\bar{p}$
0.15	0.5	0.5	0.3	0.4	1.2	2.5
0.45	1.6	1.6	0.7	1.4	4.2	12.4
0.75	2.9	2.9	1.2	2.6	7.4	9.0

after the spectrometer and vetoed themselves in the downstream Čerenkov counter. This correction was measured by running with the Čerenkov counter out of hardware veto but with such events tagged for computer analysis.

The absolute normalization depends on the density of the liquid hydrogen in our target. This was determined to be 0.0708 ± 0.0005 g/cm^3 using the measured pressure of the liquid in the refrigerator reservoir.[28] The ±0.7% uncertainty is mostly due to the ±2-psia variation in the pressure during the course of the run, with corrections for bubbles and for the normal-hydrogen to equilibrium-hydrogen conversion being much smaller.

The total effective pathlength of the incident beam in hydrogen was reduced by 0.3% because some beam particles could escape through the target walls. In principle, if the incident particles never scattered upstream of the target, we could have determined this correction from the measured distribution of the beam tracks. In practice, the most sensitive way to measure this effect was to isolate elastic scatters in the walls of the hydrogen target using target-empty data. The background from wall interactions corresponded to 0.05% of the hydrogen cross sections, and knowing the thickness of the walls, we obtained the escape correction. This 0.05% background was the only target-empty correction required. The rest of the target-empty cross section was consistent with interactions in the residual gas once the vertex fiducial cuts were made. Occasionally an event was lost when a fast δ ray from the target struck one of the veto counters lining the magnet pole faces. This effect was measured in special runs with these counters out of hardware veto, having the veto counters tagged for each event. The effect was found to be 3.8%, 2.8%, and 0.8% for pion, kaon, and proton events, respectively, independent of momentum.

Because the positive and negative beams had equal intensities, rate effects such as accidental vetoes did not affect the particle-antiparticle comparison, but only the over-all normalizations. Although individual effects were as high as 3%, as indicated by continuously monitoring delayed coincidences, beam accidentals and accidental vetoes tended to cancel. This then resulted in a 1.3% over-all normalization correction. Wide variations were made in the incident beam intensity, and it was found that the over-all reconstruction efficiency did not change by more than 2%, up to intensities of 300 000 particles/pulse.

Radiative corrections were not applied to the final cross sections. Sogard[29] has calculated these corrections for $\pi^{\pm}p$ cross sections, assuming an experimental missing-mass cut $M_x^2 < 1.16$ GeV^2; since our cutoffs were generally higher (1.15 to 1.34 GeV^2, depending on momentum), these calculations provide an upper limit for the corrections to our data. The calculations indicate that at 3 GeV/c our uncorrected cross sections are too small by 1.5% at $-t = 0.1$ and 4% at $-t = 1$ GeV^2. The difference between π^+ and π^- corrections is considerably smaller.

In summary, significant corrections for such effects as electron contamination and veto biases were measured experimentally. Calculable corrections due to decays in flight and interactions were checked against the percentage of beam triggers that failed to reconstruct with the correct momentum. Based on this comparison, an addi-

TABLE IV. Estimates of the major uncertainties in both absolute and relative particle-antiparticle normalizations.

	For absolute normalization	For relative normalization
Geometry	±2%	0
Event reconstruction efficiency	±2%	±1%
Background under M_p^2 peak (3-GeV/c π^+,K^+)	±0.5% (±1%)	±0.3% (±1%)
Nuclear absorption ($\bar{p}$;$\bar{p}/p$)	±1% (±2%)	±0.4% (±1%)
K decays at 3 and 6 GeV/c	±2.6%, ±1.3%	0
μ, e contamination (π's only)	±1.5%	±0.5%
Rate effects	±1.5%	±0.3%
δ-ray vetoes	±0.7%	0
Liquid hydrogen density	±0.7%	0

tional correction for reconstruction inefficiency of $(2 \pm 1)\%$ was applied to all reactions studied. A summary of the more important uncertainties is shown in Table IV. The over-all absolute normalization uncertainty is about $\pm 4\%$, while the particle-antiparticle relative normalization is $\pm 1.5\%$.

D. Coulomb interference corrections

At small t the interference between the single Coulomb scattering amplitude and the nuclear amplitude is important. To correct for this effect we used the formula[30]

$$\frac{d\sigma}{dt}(x^{\pm}p) = \frac{F_C^2}{t^2} \mp \frac{2F_C}{|t|} f_I(\alpha_{\pm}\cos\epsilon \pm \sin\epsilon) + (1+\alpha_{\pm}^2) f_I^2 , \quad (1)$$

where the values used for $\alpha_{\pm}$, the real-to-imaginary ratio for forward $x^{\pm}p$ elastic scattering, are shown in Table V.[31-35] The Coulomb amplitude is given by

$$F_C = \frac{2\sqrt{\pi}}{137\beta} \frac{G_x(t)G_p(t)}{1-|t|/4M_p^2}, \quad (2)$$

where β is the laboratory velocity of the incident beam. Ignoring the t dependence of the denominator and taking $G(t)$ to be the dipole form factor for both $x^{\pm}$ and proton, we see that

$$F_C = \frac{0.01613/\beta}{(1+|t|/0.71)^4} \text{ mb}^{1/2}\,\text{GeV}. \quad (3)$$

Following West and Yennie,[36] the small phase of the Coulomb amplitude was calculated to be

$$\epsilon = -(\ln B'|t| + 0.577)/137\beta , \quad (4)$$

where B' is related to the slope B of the elastic scattering diffraction peak by

$$B' = \tfrac{1}{2}B + 4 \text{ GeV}^{-2}. \quad (5)$$

The imaginary part of the nuclear amplitude was parameterized as

$$f_I = \frac{\sigma_{\text{tot}}}{4.42} e^{Bt/2} \text{ (mb/GeV}^2)^{1/2}, \quad (6)$$

with the σ_{tot}'s listed in Table VI, and B calculated directly from the data. Small-t corrections are shown in Table VII for the 3-GeV/c case; the corrections were largest for positive-particle scattering, the worst case being the K^+ correction of -11% at $-t = 0.025$ GeV^2.

IV. RESULTS

A. Cross sections

The differential cross sections for all six reactions are shown in Fig. 3 for incident laboratory momenta of 3, 3.65, 5, and 6 GeV/c. All corrections discussed in Sec. III have been applied except for the radiative corrections. The data points indicated by squares at $t = 0$ in this and in subsequent figures were derived via the optical theorem from the real-to-imaginary ratios and total cross sections shown in Tables V and VI. The data shown in Fig. 3 are also tabulated in Table VIII; the same data are presented in Table IX for larger bins. The errors principally represent the statistical uncertainties and, at small t, the uncertainty in the Coulomb interference correction; the $\pm 4\%$ uncertainty in over-all normalization is not shown.

B. Exponential fits

Least-squares fits to the form

$$\frac{d\sigma}{dt} = Ae^{Bt} \quad (7)$$

were made to the $\pi^{\pm}$ and $K^{\pm}$ data over the interval $0.05 < -t < 0.44$ GeV^2. The lower limit was chosen to avoid possible systematic effects such as those arising from the Coulomb corrections. The upper

TABLE V. Values of α, the real-to-imagninary ratio at $t = 0$, used to calculate the expected forward cross sections (from the optical theorem) as well as the corrections for interference with single Coulomb scattering. The pion values were taken from the tables of Höhler and Strauss (Ref. 31), and the K^+ values from the dispersion calculations of Lusignoli *et al.* (Ref. 32). The α's taken for K^- scattering were a compromise between $\alpha \approx 0$ of most dispersion calculations and the measured 4.2 GeV/c value of 0.20 ± 0.07 (Ref. 33). The proton and antiproton values were taken from the tables of Giacomelli (Ref. 34), in agreement with the dispersion calculation of Söding (Ref. 35). The errors represent our somewhat generous estimate of the uncertainties.

p (GeV/c)	π^+	π^-	K^+	K^-	p	$\bar{p}$
3	-0.33 ± 0.06	-0.16 ± 0.04	-0.45 ± 0.15	0.08 ± 0.10	-0.29 ± 0.06	0.05 ± 0.10
3.65	-0.31 ± 0.06	-0.17 ± 0.04	-0.39 ± 0.15	0.08 ± 0.10	-0.32 ± 0.06	0.01 ± 0.10
5	-0.29 ± 0.06	-0.15 ± 0.04	-0.30 ± 0.15	0.08 ± 0.10	-0.33 ± 0.06	-0.03 ± 0.10
6	-0.27 ± 0.06	-0.14 ± 0.04	-0.28 ± 0.15	0.08 ± 0.10	-0.32 ± 0.06	-0.04 ± 0.10

TABLE VI. Values of σ_{tot} (mb) used to calculate the expected elastic scattering cross section at $t=0$ (from the compilation of Giacomelli, Ref. 34).

p (GeV/c)	π^+	π^-	K^+	K^-	p	$\bar{p}$
3	28.8±0.3	32.2±0.3	17.2±0.1	27.4±0.2	44.45±0.05	76.70±0.05
3.65	28.0±0.3	31.0±0.3	17.1±0.2	26.2±0.3	42.82±0.05	70.6±0.5
5	26.5±0.3	29.1±0.3	17.1±0.2	24.9±0.3	41.20±0.05	63.1±1.0
6	25.8±0.3	28.2±0.3	17.1±0.2	24.2±0.3	40.75±0.10	60.1±1.0

cutoff of 0.44 GeV^2 was also chosen conservatively to avoid bias. The pion and kaon data generally appear consistent with the extrapolation of these fits out to $-t=0.6$ GeV^2, as shown in Fig. 3. To obtain reasonable exponential fits to the wider interval $0.05<-t<1.0$ GeV^2 one must use a cubic term for $\pi^{\pm}$ and a quadratic term for K^-; linear fits to the K^+ data are good over the entire interval.

The pp and $\bar{p}p$ data are not well fitted by Eq. (7), but appear to have curvature everywhere. They were fitted to

$$\frac{d\sigma}{dt}=Ae^{Bt+Ct^2}. \tag{8}$$

This form reproduces the $\bar{p}p$ data out to about 0.5 GeV^2 (0.05 to 0.44 GeV^2 was used in the fits), beyond which there is a sharp break followed by a shallow secondary peak near $-t=0.8$ GeV^2. The pp data follow the quadratic form out to about 1.5 GeV^2 (0.05 to 1.0 GeV^2 was used in the fits).

The results of the fits are shown in Fig. 3 and summarized in Table X. The χ^2's indicate that the data are in general well fitted by these simple forms. Adding together the results from all four momenta yields χ^2 probabilities of 53%, 1.4%, 14%, 37%, 73%, and 43% for π^+, π^-, K^+, K^-, p, and $\bar{p}$, respectively. The worst fits are for the 5- and 6-GeV/c π^- data, each with a χ^2 probability of about 3%; in both cases the large χ^2 can be attributed to a single point ($-t=0.35$ and 0.095 GeV^2 for the respective momenta) about 3.7 standard deviations low.

C. Comparison with optical point

The values obtained for the parameter A (the $t=0$ cross section) from the exponential fits generally agree with those expected from the optical theorem. Figure 4 shows

$$1+\alpha^2=A\Big/\left(\frac{d\sigma}{dt}\right)_{\text{O.T.}}, \tag{9}$$

where the optical-theorem cross section is calculated from the total cross sections shown in Table VI using

$$\left(\frac{d\sigma}{dt}\right)_{\text{O.T.}}=\frac{\sigma_{tot}^2}{19.58} \tag{10}$$

(units of mb and GeV^2). Various dispersion-relation predictions for $1+\alpha^2$ are also shown in Fig. 4. The pion extrapolations agree well with expectations (with the possible exception of the 3-GeV/c π^+ point) and there appears to be no need for a break in these distributions at small t.[37,38] Our values of α^2 for K^+ are somewhat lower than most dispersion-relation predictions (for example those of Martin and Poole[39]), but are in agreement with calculations such as those of Lusignoli *et al.*[32] The K^- extrapolations at 5 and 6 GeV/c seem about 10% low. A similar effect found by Henzi *et al.*[40] in high-energy (>7 GeV/c) K^-p data was ascribed to an upward curvature at small t.

D. Comparison with previous experiments

The 5-GeV/c data of this experiment are compared in Fig. 5 with previous experiments. The

TABLE VII. Corrections (percent) applied to the small-t 3-GeV/c data to eliminate Coulomb interference effects.

$-t$ (GeV^2)	π^+	π^-	K^+	K^-	p	$\bar{p}$
0.025	−5.7±0.7	2.1±0.7	−11.2±1.9	−2.4±1.9	−3.5±0.5	−0.5±0.8
0.035	−3.9±0.5	1.6±0.5	−7.6±1.4	−1.5±1.3	−2.4±0.4	−0.3±0.6
0.045	−3.0±0.4	1.3±0.3	−5.7±1.1	−1.1±1.0	−1.8±0.3	−0.3±0.4
0.055	−2.4±0.3	1.0±0.3	−4.5±0.9	−0.9±0.8	−1.5±0.2	−0.2±0.4
0.065	−1.9±0.3	0.9±0.2	−3.6±0.8	−0.7±0.7	−1.2±0.2	−0.2±0.3

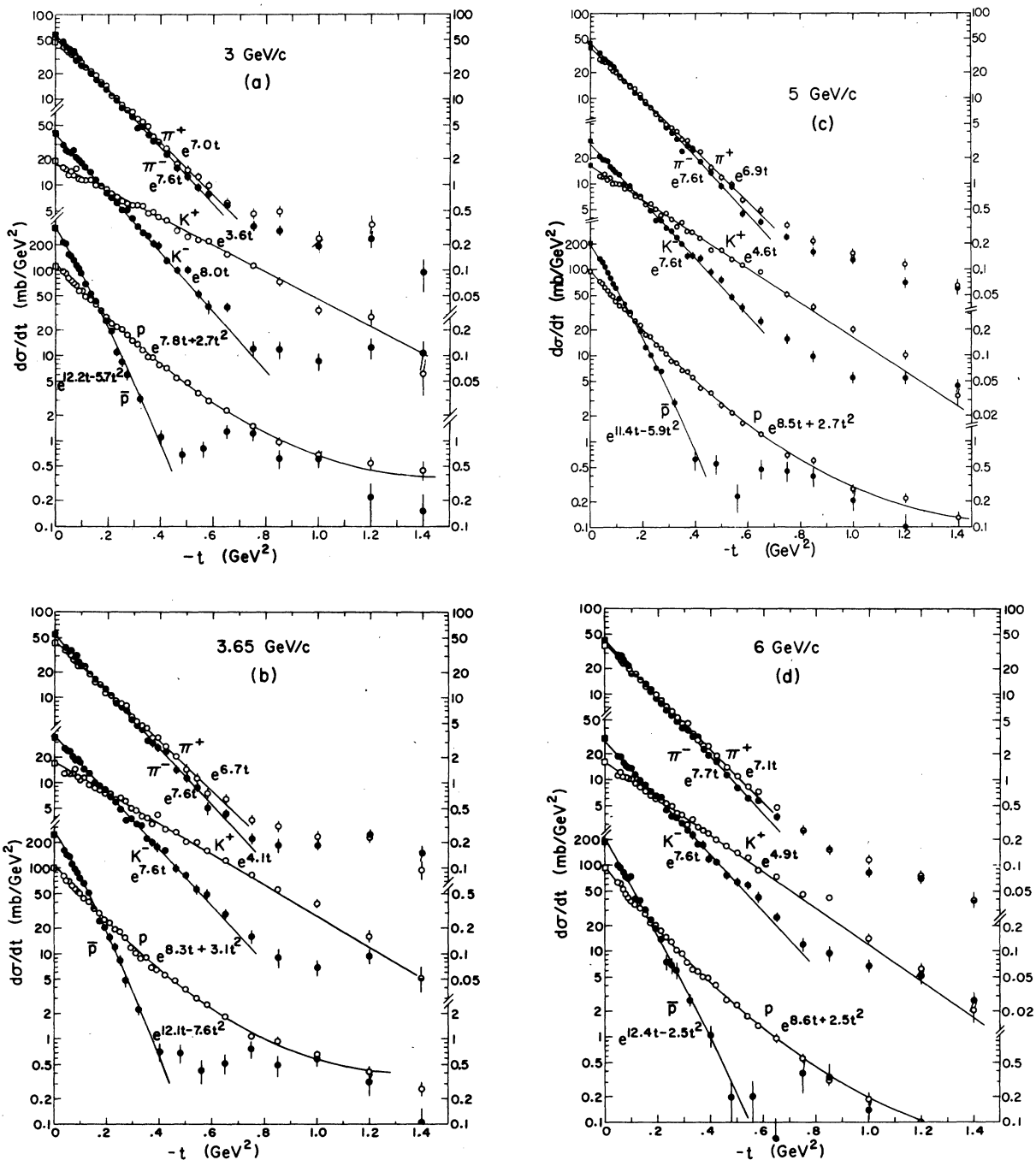

FIG. 3. Differential cross sections for the elastic scattering of six different particles from protons. The square points at $t = 0$ were derived via the optical theorem from previous measurements. The parameters for the fitted curves are given in Table X. The incident beam momenta are (a) 3 GeV/c, (b) 3.65 GeV/c. (c) 5 GeV/c, and (d) 6 GeV/c.

bubble-chamber experiments of MacNaughton *et al.*,[10] De Baere *et al.*,[11] Mott *et al.*,[14] and Böckmann *et al.*[17] are generally in agreement with this experiment, although their statistical errors are somewhat large. The K^- bubble-chamber experiment of Aguilar-Benitez[13] is about 40% higher. The counter experiments of Coffin *et al.*,[9] Rust *et al.*,[8] and Akerlof *et al.*[12] agree well with this experiment. The high-statistics proton data of Clyde[16] are in fair agreement (10% or 20% high in some t regions), and the K^- data of Owen *et al.*[15] seem 40% low. The final results of Chabaud *et al.*,[7]

TABLE VIII. Differential cross sections for elastic scattering from protons (mb/GeV^2) as a function of t (GeV^2). The errors shown include statistical errors and the uncertainty in the single Coulomb interference correction, but not the ±4% uncertainty of over-all normalization. Radiative corrections have not been made (Ref. 29). The $t = 0$ values were derived from the real-to-imaginary ratios and cross sections listed in Tables V and VI.

$-t$	π^+	π^-	K^+	K^-	p	$\bar{p}$
			(a) 3 GeV/c			
0.000	47.1 ± 1.9	54.5 ± 1.2	18.4 ± 2.1	38.8 ± 0.9	109.6 ± 3.5	303.2 ± 4.3
0.025	41.8 ± 2.4	48.1 ± 2.3	16.2 ± 1.3	29.5 ± 1.8	98.9 ± 3.9	213.9 ± 11.8
0.035	39.2 ± 2.6	42.1 ± 2.3	15.6 ± 1.4	25.5 ± 1.8	93.2 ± 4.2	208.5 ± 12.6
0.045	35.8 ± 1.6	38.2 ± 1.4	13.19 ± 0.81	24.3 ± 1.1	81.9 ± 2.5	154.0 ± 7.0
0.055	32.8 ± 1.4	36.5 ± 1.3	14.73 ± 0.80	23.8 ± 1.0	77.7 ± 2.3	147.8 ± 6.4
0.065	35.1 ± 1.5	37.3 ± 1.3	13.02 ± 0.75	25.5 ± 1.0	71.5 ± 2.2	131.7 ± 5.9
0.075	31.0 ± 1.4	29.1 ± 1.1	15.56 ± 0.82	21.21 ± 0.95	67.5 ± 2.1	114.0 ± 5.5
0.085	29.7 ± 1.3	29.6 ± 1.1	12.13 ± 0.72	19.47 ± 0.90	58.3 ± 1.9	104.8 ± 5.3
0.095	27.0 ± 1.3	24.8 ± 1.0	11.59 ± 0.70	18.04 ± 0.86	58.1 ± 1.9	92.8 ± 4.9
0.110	23.39 ± 0.84	24.37 ± 0.73	11.26 ± 0.49	16.13 ± 0.58	49.5 ± 1.3	68.9 ± 3.0
0.13	21.69 ± 0.81	20.96 ± 0.68	11.46 ± 0.49	14.05 ± 0.54	45.1 ± 1.2	53.2 ± 2.6
0.15	19.31 ± 0.76	17.04 ± 0.61	10.02 ± 0.46	11.51 ± 0.48	39.8 ± 1.1	43.4 ± 2.4
0.17	15.85 ± 0.69	15.51 ± 0.58	9.79 ± 0.46	9.71 ± 0.44	34.5 ± 1.1	33.4 ± 2.1
0.19	14.55 ± 0.66	13.20 ± 0.54	8.97 ± 0.44	8.08 ± 0.40	28.52 ± 0.96	26.0 ± 1.8
0.21	11.00 ± 0.58	11.25 ± 0.50	7.97 ± 0.41	7.05 ± 0.38	23.89 ± 0.88	19.5 ± 1.6
0.23	10.38 ± 0.56	9.77 ± 0.46	7.23 ± 0.39	6.13 ± 0.35	21.91 ± 0.84	10.9 ± 1.2
0.25	8.70 ± 0.51	8.15 ± 0.42	6.47 ± 0.37	5.05 ± 0.32	20.67 ± 0.82	8.5 ± 1.1
0.27	7.61 ± 0.48	7.50 ± 0.40	6.17 ± 0.36	5.05 ± 0.32	17.73 ± 0.76	6.02 ± 0.89
0.29	7.18 ± 0.47	6.28 ± 0.37	5.87 ± 0.35	4.02 ± 0.28	15.16 ± 0.70	3.74 ± 0.70
0.31	5.97 ± 0.43	4.62 ± 0.32	5.83 ± 0.35	3.25 ± 0.26	13.68 ± 0.67	4.31 ± 0.77
0.33	5.46 ± 0.41	4.75 ± 0.32	5.64 ± 0.35	2.76 ± 0.24	11.76 ± 0.63	3.29 ± 0.67
0.35	4.87 ± 0.39	3.85 ± 0.29	4.62 ± 0.31	2.53 ± 0.23	9.73 ± 0.57	1.30 ± 0.41
0.37	3.66 ± 0.34	3.24 ± 0.27	4.90 ± 0.33	2.03 ± 0.20	9.61 ± 0.57	1.19 ± 0.39
0.39	3.20 ± 0.32	3.08 ± 0.26	4.25 ± 0.30	1.94 ± 0.20	7.87 ± 0.52	2.16 ± 0.54
0.42	2.67 ± 0.21	2.27 ± 0.16	3.90 ± 0.21	1.29 ± 0.12	7.15 ± 0.36	0.53 ± 0.19
0.46	1.76 ± 0.17	1.60 ± 0.14	2.94 ± 0.18	1.01 ± 0.11	5.58 ± 0.32	0.60 ± 0.21
0.50	1.49 ± 0.16	1.24 ± 0.12	2.51 ± 0.17	1.01 ± 0.11	4.93 ± 0.30	0.80 ± 0.24
0.54	1.24 ± 0.15	0.93 ± 0.11	2.27 ± 0.17	0.521 ± 0.077	3.70 ± 0.27	0.57 ± 0.21
0.58	0.98 ± 0.14	0.78 ± 0.10	2.21 ± 0.17	0.371 ± 0.067	2.99 ± 0.25	1.15 ± 0.31
0.65	0.614 ± 0.077	0.489 ± 0.054	1.532 ± 0.095	0.367 ± 0.045	2.34 ± 0.15	1.31 ± 0.22
0.75	0.460 ± 0.072	0.329 ± 0.047	1.130 ± 0.086	0.121 ± 0.027	1.52 ± 0.13	1.24 ± 0.23
0.85	0.494 ± 0.080	0.290 ± 0.047	0.742 ± 0.075	0.119 ± 0.029	0.99 ± 0.11	0.62 ± 0.17
0.95	0.211 ± 0.062	0.147 ± 0.036	0.374 ± 0.058	0.083 ± 0.026	0.77 ± 0.11	0.73 ± 0.19
1.05	0.260 ± 0.083	0.247 ± 0.059	0.313 ± 0.065	0.089 ± 0.032	0.64 ± 0.12	0.52 ± 0.20
1.15	0.382 ± 0.118	0.391 ± 0.091	0.351 ± 0.087	0.143 ± 0.052	0.82 ± 0.17	0.12 ± 0.09
1.25	0.313 ± 0.114	0.138 ± 0.054	0.234 ± 0.072	0.109 ± 0.046	0.38 ± 0.12	0.41 ± 0.22
1.35	0.022 ± 0.063	0.118 ± 0.055	0.124 ± 0.056	0.087 ± 0.045	0.42 ± 0.13	0.30 ± 0.19
1.45	0.111 ± 0.126	0.077 ± 0.056		0.134 ± 0.080	0.50 ± 0.21	
			(b) 3.65 GeV/c			
0.000	43.8 ± 1.7	50.3 ± 1.1	17.4 ± 1.8	35.6 ± 1.0	103.4 ± 3.6	256.2 ± 4.4
0.035	35.5 ± 2.1	37.8 ± 2.2	12.7 ± 1.1	25.0 ± 1.6	80.9 ± 3.8	160.1 ± 10.9
0.045	33.7 ± 1.5	32.9 ± 1.4	13.12 ± 0.85	23.4 ± 1.1	71.9 ± 2.6	143.0 ± 7.4
0.055	32.0 ± 1.3	34.3 ± 1.4	12.97 ± 0.78	23.6 ± 1.0	70.4 ± 2.3	137.4 ± 6.8
0.065	27.7 ± 1.2	29.7 ± 1.2	12.98 ± 0.77	20.30 ± 0.94	63.0 ± 2.2	112.0 ± 6.0
0.075	26.7 ± 1.2	30.4 ± 1.3	14.49 ± 0.82	18.40 ± 0.89	59.6 ± 2.2	98.4 ± 5.6
0.085	23.4 ± 1.1	26.2 ± 1.2	11.81 ± 0.73	18.55 ± 0.90	55.0 ± 2.0	89.0 ± 5.4
0.095	24.1 ± 1.1	23.6 ± 1.1	10.93 ± 0.70	17.42 ± 0.86	51.4 ± 1.9	77.4 ± 5.0
0.11	22.87 ± 0.79	23.39 ± 0.79	11.49 ± 0.51	14.59 ± 0.55	45.1 ± 1.3	66.7 ± 3.2
0.13	19.07 ± 0.72	19.06 ± 0.71	9.44 ± 0.46	12.85 ± 0.52	40.7 ± 1.2	51.5 ± 2.8

TABLE VIII *(Continued)*

$-t$	π^+	π^-	K^+	K^-	p	$\bar{p}$
			(b) 3.65 GeV/c			
0.15	15.65 ± 0.65	16.20 ± 0.66	8.66 ± 0.44	9.97 ± 0.45	33.6 ± 1.1	33.9 ± 2.3
0.17	14.19 ± 0.62	14.01 ± 0.61	8.49 ± 0.44	9.28 ± 0.44	30.1 ± 1.0	24.5 ± 1.9
0.19	11.49 ± 0.56	12.60 ± 0.58	7.60 ± 0.41	8.39 ± 0.42	25.26 ± 0.99	20.2 ± 1.7
0.21	10.78 ± 0.54	10.86 ± 0.54	7.32 ± 0.41	6.85 ± 0.38	23.19 ± 0.95	15.6 ± 1.5
0.23	9.07 ± 0.49	8.56 ± 0.48	6.33 ± 0.38	5.94 ± 0.35	19.62 ± 0.87	12.0 ± 1.3
0.25	8.56 ± 0.48	7.57 ± 0.45	6.59 ± 0.38	4.91 ± 0.32	18.24 ± 0.84	8.3 ± 1.1
0.27	8.09 ± 0.47	6.98 ± 0.43	6.11 ± 0.37	3.62 ± 0.27	15.66 ± 0.78	4.84 ± 0.87
0.29	5.94 ± 0.40	5.45 ± 0.38	5.05 ± 0.33	3.80 ± 0.28	11.84 ± 0.68	5.13 ± 0.90
0.31	5.36 ± 0.38	4.75 ± 0.35	4.80 ± 0.32	3.29 ± 0.26	10.29 ± 0.64	2.68 ± 0.65
0.33	4.75 ± 0.36	4.24 ± 0.33	4.05 ± 0.30	3.16 ± 0.25	8.86 ± 0.59	1.55 ± 0.49
0.35	4.44 ± 0.35	3.13 ± 0.29	3.87 ± 0.29	2.20 ± 0.21	9.13 ± 0.60	1.13 ± 0.41
0.37	3.37 ± 0.30	2.91 ± 0.28	3.30 ± 0.27	1.98 ± 0.20	6.91 ± 0.52	1.00 ± 0.39
0.39	3.39 ± 0.30	2.58 ± 0.26	4.22 ± 0.31	1.78 ± 0.19	6.59 ± 0.51	1.01 ± 0.39
0.42	2.71 ± 0.19	2.36 ± 0.18	2.86 ± 0.18	1.62 ± 0.13	5.63 ± 0.34	0.49 ± 0.19
0.46	2.06 ± 0.17	1.41 ± 0.14	2.68 ± 0.17	0.99 ± 0.10	4.83 ± 0.32	0.64 ± 0.23
0.50	1.46 ± 0.14	1.16 ± 0.12	2.05 ± 0.15	0.834 ± 0.096	3.90 ± 0.29	0.73 ± 0.25
0.54	1.14 ± 0.13	0.88 ± 0.11	2.02 ± 0.15	0.570 ± 0.080	3.05 ± 0.26	0.51 ± 0.20
0.58	0.75 ± 0.10	0.503 ± 0.086	1.60 ± 0.14	0.499 ± 0.075	2.54 ± 0.23	0.36 ± 0.17
0.65	0.642 ± 0.063	0.439 ± 0.052	1.243 ± 0.080	0.294 ± 0.037	1.85 ± 0.13	0.52 ± 0.14
0.75	0.370 ± 0.050	0.221 ± 0.038	0.849 ± 0.069	0.161 ± 0.028	1.09 ± 0.10	0.78 ± 0.17
0.85	0.311 ± 0.048	0.186 ± 0.036	0.576 ± 0.059	0.091 ± 0.022	0.95 ± 0.10	0.49 ± 0.14
0.95	0.353 ± 0.054	0.164 ± 0.036	0.435 ± 0.055	0.079 ± 0.022	0.685 ± 0.093	0.73 ± 0.18
1.05	0.158 ± 0.038	0.213 ± 0.043	0.345 ± 0.051	0.061 ± 0.020	0.654 ± 0.095	0.48 ± 0.15
1.15	0.271 ± 0.052	0.283 ± 0.053	0.151 ± 0.035	0.120 ± 0.030	0.434 ± 0.081	0.42 ± 0.15
1.25	0.203 ± 0.047	0.218 ± 0.048	0.175 ± 0.040	0.074 ± 0.024	0.402 ± 0.083	0.24 ± 0.11
1.35	0.085 ± 0.031	0.165 ± 0.044	0.104 ± 0.032	0.111 ± 0.032	0.255 ± 0.067	0.13 ± 0.08
1.45	0.110 ± 0.040	0.138 ± 0.045	0.027 ± 0.016	0.024 ± 0.014	0.276 ± 0.081	0.09 ± 0.06
1.55	0.204 ± 0.070	0.149 ± 0.058	0.114 ± 0.047	0.081 ± 0.037	0.159 ± 0.071	
1.65	0.062 ± 0.037		0.027 ± 0.019	0.097 ± 0.044	0.086 ± 0.054	
1.75	0.169 ± 0.072		0.030 ± 0.022	0.135 ± 0.057	0.144 ± 0.078	
			(c) 5 GeV/c			
0.000	38.9 ± 1.5	44.3 ± 1.0	16.5 ± 1.4	31.97 ± 0.97	96.3 ± 3.4	204.8 ± 6.9
0.035	28.7 ± 1.2	34.5 ± 1.2	12.49 ± 0.80	21.01 ± 0.98	73.1 ± 2.6	135.6 ± 8.0
0.045	27.44 ± 0.96	28.77 ± 0.90	12.22 ± 0.64	19.05 ± 0.75	68.3 ± 2.1	122.4 ± 6.2
0.055	26.90 ± 0.88	29.12 ± 0.84	13.08 ± 0.61	18.96 ± 0.69	62.1 ± 1.8	107.1 ± 5.4
0.065	26.67 ± 0.87	26.13 ± 0.79	11.22 ± 0.56	18.40 ± 0.67	56.7 ± 1.8	93.2 ± 5.0
0.075	22.93 ± 0.81	26.02 ± 0.78	11.75 ± 0.57	15.97 ± 0.62	51.3 ± 1.7	79.9 ± 4.6
0.085	21.24 ± 0.78	23.94 ± 0.75	10.08 ± 0.52	14.71 ± 0.59	48.5 ± 1.6	67.9 ± 4.2
0.095	20.01 ± 0.75	20.99 ± 0.70	10.18 ± 0.52	13.88 ± 0.57	42.4 ± 1.5	60.6 ± 4.0
0.11	17.63 ± 0.50	18.24 ± 0.46	9.93 ± 0.36	12.88 ± 0.39	38.2 ± 1.0	46.0 ± 2.4
0.13	16.24 ± 0.48	16.00 ± 0.43	8.81 ± 0.34	10.20 ± 0.34	34.80 ± 0.99	40.0 ± 2.3
0.15	13.72 ± 0.44	14.27 ± 0.40	8.75 ± 0.34	9.55 ± 0.33	30.15 ± 0.92	31.9 ± 2.0
0.17	12.94 ± 0.42	11.69 ± 0.36	7.14 ± 0.31	7.53 ± 0.29	25.17 ± 0.84	25.0 ± 1.8
0.19	11.25 ± 0.40	10.26 ± 0.34	6.97 ± 0.30	7.13 ± 0.28	22.78 ± 0.80	19.1 ± 1.5
0.21	9.29 ± 0.36	8.72 ± 0.31	5.75 ± 0.27	5.88 ± 0.26	17.48 ± 0.70	12.6 ± 1.3
0.23	7.87 ± 0.33	7.86 ± 0.30	5.86 ± 0.27	4.88 ± 0.23	16.82 ± 0.69	10.1 ± 1.1
0.25	6.51 ± 0.30	6.74 ± 0.27	5.03 ± 0.25	3.76 ± 0.20	13.40 ± 0.61	7.14 ± 0.98
0.27	5.71 ± 0.28	5.58 ± 0.25	4.29 ± 0.23	3.68 ± 0.20	12.06 ± 0.58	6.51 ± 0.93
0.29	4.96 ± 0.26	4.53 ± 0.22	4.53 ± 0.24	3.01 ± 0.18	10.47 ± 0.54	5.52 ± 0.85
0.31	4.50 ± 0.25	3.95 ± 0.21	3.81 ± 0.22	2.78 ± 0.17	8.55 ± 0.49	3.53 ± 0.69
0.33	4.12 ± 0.24	3.33 ± 0.19	3.15 ± 0.20	2.36 ± 0.16	8.05 ± 0.48	2.46 ± 0.57
0.35	3.30 ± 0.21	2.39 ± 0.16	3.52 ± 0.21	1.99 ± 0.15	6.75 ± 0.44	1.29 ± 0.41

TABLE VIII *(Continued)*

$-t$	π^+	π^-	K^+	K^-	p	$\bar{p}$
			(c) 5 GeV/c			
0.37	3.18 ± 0.21	2.80 ± 0.18	2.78 ± 0.19	1.45 ± 0.12	6.47 ± 0.43	0.82 ± 0.32
0.39	2.45 ± 0.18	2.58 ± 0.17	2.72 ± 0.19	1.44 ± 0.12	5.54 ± 0.40	0.94 ± 0.34
0.42	2.34 ± 0.13	1.81 ± 0.10	2.32 ± 0.12	1.349 ± 0.088	4.19 ± 0.24	0.40 ± 0.16
0.46	1.54 ± 0.10	1.341 ± 0.089	1.69 ± 0.10	0.936 ± 0.074	3.64 ± 0.23	0.87 ± 0.24
0.50	1.188 ± 0.094	0.934 ± 0.075	1.67 ± 0.10	0.760 ± 0.067	2.64 ± 0.19	0.35 ± 0.15
0.54	0.993 ± 0.087	0.923 ± 0.075	1.313 ± 0.096	0.475 ± 0.053	2.15 ± 0.18	0.17 ± 0.10
0.58	0.655 ± 0.071	0.444 ± 0.052	1.133 ± 0.090	0.360 ± 0.047	1.66 ± 0.16	0.30 ± 0.14
0.65	0.490 ± 0.039	0.353 ± 0.030	0.940 ± 0.052	0.248 ± 0.025	1.227 ± 0.089	0.47 ± 0.12
0.75	0.328 ± 0.033	0.239 ± 0.025	0.508 ± 0.039	0.157 ± 0.020	0.687 ± 0.068	0.44 ± 0.11
0.85	0.214 ± 0.027	0.159 ± 0.021	0.365 ± 0.034	0.097 ± 0.016	0.598 ± 0.065	0.39 ± 0.10
0.95	0.168 ± 0.024	0.138 ± 0.020	0.204 ± 0.026	0.043 ± 0.011	0.337 ± 0.049	0.203 ± 0.076
1.05	0.146 ± 0.023	0.123 ± 0.019	0.196 ± 0.026	0.072 ± 0.014	0.226 ± 0.041	0.213 ± 0.080
1.15	0.124 ± 0.021	0.082 ± 0.016	0.119 ± 0.020	0.063 ± 0.014	0.197 ± 0.039	0.310 ± 0.099
1.25	0.106 ± 0.020	0.059 ± 0.013	0.085 ± 0.017	0.048 ± 0.012	0.234 ± 0.043	0.032 ± 0.024
1.35	0.066 ± 0.016	0.079 ± 0.016	0.045 ± 0.013	0.038 ± 0.011	0.131 ± 0.033	
1.45	0.063 ± 0.016	0.044 ± 0.012	0.024 ± 0.009	0.051 ± 0.013	0.125 ± 0.033	
1.55	0.059 ± 0.016	0.055 ± 0.014	0.018 ± 0.008	0.034 ± 0.011	0.052 ± 0.021	
1.65	0.049 ± 0.015	0.047 ± 0.014	0.014 ± 0.007	0.024 ± 0.009	0.055 ± 0.023	
1.75	0.005 ± 0.004	0.038 ± 0.012	0.010 ± 0.006	0.009 ± 0.005	0.059 ± 0.025	
1.85	0.040 ± 0.015	0.019 ± 0.009	0.011 ± 0.007	0.014 ± 0.007	0.043 ± 0.021	
1.95	0.037 ± 0.014	0.035 ± 0.013	0.012 ± 0.007	0.020 ± 0.009	0.046 ± 0.022	
			(d) 6 GeV/c			
0.000	36.6 ± 1.4	41.57 ± 0.99	16.3 ± 1.3	30.25 ± 0.93	93.6 ± 3.3	185.9 ± 6.6
0.045	27.86 ± 0.95	27.96 ± 0.79	11.42 ± 0.64	18.81 ± 0.90	62.8 ± 1.9	99.6 ± 8.7
0.055	25.03 ± 0.84	28.08 ± 0.73	12.36 ± 0.61	18.84 ± 0.84	61.4 ± 1.7	96.1 ± 7.9
0.065	23.94 ± 0.81	24.49 ± 0.67	10.93 ± 0.57	15.99 ± 0.76	52.7 ± 1.6	84.0 ± 7.4
0.075	21.98 ± 0.78	22.31 ± 0.64	10.86 ± 0.56	14.59 ± 0.72	46.2 ± 1.5	74.0 ± 6.9
0.085	19.59 ± 0.73	21.36 ± 0.62	10.59 ± 0.55	13.93 ± 0.70	42.3 ± 1.4	71.7 ± 6.8
0.095	18.43 ± 0.71	17.31 ± 0.56	10.52 ± 0.54	13.96 ± 0.70	38.9 ± 1.4	75.1 ± 6.9
0.11	17.71 ± 0.49	17.06 ± 0.39	9.11 ± 0.36	11.58 ± 0.45	35.57 ± 0.95	40.5 ± 3.6
0.13	14.53 ± 0.44	14.80 ± 0.36	8.10 ± 0.34	9.75 ± 0.41	31.56 ± 0.89	38.0 ± 3.5
0.15	12.26 ± 0.41	13.18 ± 0.34	7.45 ± 0.32	8.64 ± 0.38	27.25 ± 0.83	30.1 ± 3.1
0.17	11.37 ± 0.39	10.81 ± 0.31	6.65 ± 0.30	7.27 ± 0.35	21.74 ± 0.74	22.9 ± 2.7
0.19	9.92 ± 0.36	8.90 ± 0.28	6.20 ± 0.29	6.50 ± 0.33	20.11 ± 0.71	18.9 ± 2.4
0.21	8.48 ± 0.34	7.86 ± 0.26	5.76 ± 0.28	6.27 ± 0.33	17.38 ± 0.66	14.1 ± 2.1
0.23	7.28 ± 0.31	6.65 ± 0.24	5.24 ± 0.27	4.57 ± 0.28	14.61 ± 0.61	7.5 ± 1.5
0.25	6.29 ± 0.29	5.96 ± 0.23	4.94 ± 0.26	3.74 ± 0.25	12.90 ± 0.57	6.9 ± 1.4
0.27	5.42 ± 0.27	4.86 ± 0.20	4.05 ± 0.23	3.67 ± 0.25	10.43 ± 0.51	5.9 ± 1.3
0.29	4.56 ± 0.25	4.02 ± 0.19	3.87 ± 0.23	3.13 ± 0.23	9.34 ± 0.49	3.2 ± 1.0
0.31	4.59 ± 0.25	3.80 ± 0.18	3.00 ± 0.20	2.64 ± 0.21	7.44 ± 0.43	2.29 ± 0.84
0.33	3.41 ± 0.21	3.24 ± 0.17	3.43 ± 0.21	2.29 ± 0.19	6.14 ± 0.39	2.86 ± 0.95
0.35	2.98 ± 0.20	3.05 ± 0.16	2.82 ± 0.19	1.77 ± 0.17	5.79 ± 0.38	2.29 ± 0.83
0.37	2.48 ± 0.18	2.29 ± 0.14	2.58 ± 0.18	1.73 ± 0.17	5.09 ± 0.36	1.72 ± 0.71
0.39	2.49 ± 0.18	1.92 ± 0.13	2.39 ± 0.18	1.18 ± 0.14	4.91 ± 0.35	0.57 ± 0.36
0.42	1.91 ± 0.11	1.663 ± 0.087	2.02 ± 0.11	1.102 ± 0.098	4.05 ± 0.23	0.97 ± 0.39
0.46	1.401 ± 0.099	1.150 ± 0.072	1.71 ± 0.11	0.770 ± 0.082	2.70 ± 0.19	0.28 ± 0.18
0.50	1.104 ± 0.089	0.802 ± 0.061	1.42 ± 0.10	0.643 ± 0.075	2.37 ± 0.17	0.14 ± 0.11
0.54	0.837 ± 0.078	0.611 ± 0.054	1.244 ± 0.095	0.594 ± 0.073	1.77 ± 0.15	0.14 ± 0.11
0.58	0.734 ± 0.073	0.577 ± 0.052	0.881 ± 0.080	0.425 ± 0.062	1.35 ± 0.13	0.28 ± 0.19
0.65	0.480 ± 0.038	0.376 ± 0.027	0.749 ± 0.048	0.252 ± 0.031	0.982 ± 0.076	0.06 ± 0.05
0.75	0.265 ± 0.029	0.256 ± 0.023	0.465 ± 0.038	0.122 ± 0.022	0.579 ± 0.059	0.37 ± 0.15
0.85	0.155 ± 0.022	0.155 ± 0.018	0.426 ± 0.037	0.096 ± 0.019	0.321 ± 0.045	0.33 ± 0.14

TABLE VIII *(Continued)*

$-t$	π^+	π^-	K^+	K^-	p	$\bar{p}$
			(d) 6 GeV/c			
0.95	0.157 ± 0.023	0.086 ± 0.014	0.160 ± 0.023	0.059 ± 0.015	0.262 ± 0.041	0.07 ± 0.05
1.05	0.089 ± 0.017	0.083 ± 0.013	0.126 ± 0.021	0.077 ± 0.018	0.134 ± 0.029	0.28 ± 0.13
1.15	0.076 ± 0.016	0.073 ± 0.013	0.074 ± 0.016	0.060 ± 0.016	0.146 ± 0.031	
1.25	0.079 ± 0.017	0.073 ± 0.013	0.053 ± 0.014	0.048 ± 0.014	0.065 ± 0.021	
1.35	0.042 ± 0.012	0.055 ± 0.011	0.037 ± 0.011	0.031 ± 0.011	0.074 ± 0.022	
1.45	0.040 ± 0.012	0.028 ± 0.008	0.011 ± 0.006	0.023 ± 0.010	0.064 ± 0.021	
1.55	0.011 ± 0.006	0.027 ± 0.008	0.008 ± 0.005	0.014 ± 0.007	0.058 ± 0.020	
1.65	0.027 ± 0.010	0.015 ± 0.006	0.008 ± 0.005	0.010 ± 0.006	0.048 ± 0.019	
1.75	0.008 ± 0.005	0.024 ± 0.008	0.009 ± 0.005	0.015 ± 0.008	0.035 ± 0.016	
1.85	0.004 ± 0.003	0.008 ± 0.004	0.009 ± 0.005	0.016 ± 0.008	0.022 ± 0.012	
1.95	0.027 ± 0.011	0.015 ± 0.006				
2.05	0.005 ± 0.004	0.006 ± 0.004				

TABLE IX. Data of Table VIII combined into larger bins. p_{lab} in GeV/c; t in GeV^2; differential cross sections in mb/GeV^2.

p_{lab} \ $-t$	π^+	π^-	K^+	K^-	p	$\bar{p}$
3	0.00	47.0 ± 1.9	54.5 ± 1.2	18.3 ± 2.0	38.78 ± 0.91	109.6 ± 3.5	303.2 ± 4.2
	0.03	40.4 ± 1.7	44.9 ± 1.6	15.86 ± 0.94	27.41 ± 1.28	96.0 ± 2.8	211.1 ± 8.6
	0.06	33.68 ± 0.72	35.25 ± 0.64	14.14 ± 0.39	23.74 ± 0.51	74.4 ± 1.1	136.1 ± 3.0
	0.10	25.73 ± 0.62	25.74 ± 0.53	11.56 ± 0.35	17.38 ± 0.42	53.69 ± 0.93	82.5 ± 2.3
	0.16	17.63 ± 0.36	16.45 ± 0.30	10.02 ± 0.23	10.61 ± 0.23	36.48 ± 0.54	37.6 ± 1.1
	0.24	9.33 ± 0.26	9.05 ± 0.22	6.92 ± 0.19	5.77 ± 0.17	20.93 ± 0.41	10.24 ± 0.60
	0.32	5.81 ± 0.21	4.82 ± 0.16	5.48 ± 0.17	3.09 ± 0.12	12.42 ± 0.32	3.11 ± 0.34
	0.40	3.02 ± 0.15	2.68 ± 0.12	4.22 ± 0.15	1.604 ± 0.092	7.89 ± 0.26	1.12 ± 0.21
	0.48	1.62 ± 0.11	1.409 ± 0.092	2.71 ± 0.12	1.010 ± 0.075	5.24 ± 0.21	0.69 ± 0.15
	0.56	1.10 ± 0.10	0.853 ± 0.074	2.24 ± 0.11	0.439 ± 0.051	3.32 ± 0.18	0.80 ± 0.18
3.65	0.00	43.8 ± 1.7	50.3 ± 1.2	17.4 ± 1.8	35.65 ± 1.05	103.4 ± 3.6	256.2 ± 4.4
	0.06	29.95 ± 0.66	31.90 ± 0.68	13.37 ± 0.40	21.39 ± 0.49	66.2 ± 1.2	121.6 ± 3.2
	0.10	23.33 ± 0.56	24.17 ± 0.57	11.43 ± 0.36	16.20 ± 0.41	49.04 ± 0.98	74.4 ± 2.4
	0.16	14.86 ± 0.32	15.28 ± 0.32	8.52 ± 0.22	10.01 ± 0.23	31.98 ± 0.56	30.5 ± 1.1
	0.24	9.08 ± 0.25	8.39 ± 0.23	6.58 ± 0.19	5.20 ± 0.16	19.00 ± 0.43	9.45 ± 0.64
	0.32	5.09 ± 0.18	4.32 ± 0.17	4.42 ± 0.15	3.07 ± 0.12	9.98 ± 0.31	2.22 ± 0.31
	0.40	3.03 ± 0.14	2.54 ± 0.13	3.33 ± 0.14	1.751 ± 0.096	6.17 ± 0.25	0.71 ± 0.17
	0.48	1.73 ± 0.11	1.285 ± 0.096	2.34 ± 0.11	0.911 ± 0.071	4.34 ± 0.21	0.68 ± 0.17
	0.56	0.926 ± 0.084	0.667 ± 0.071	1.80 ± 0.10	0.533 ± 0.055	2.78 ± 0.17	0.43 ± 0.13
5	0.00	38.9 ± 1.5	44.3 ± 1.0	16.5 ± 1.4	31.97 ± 0.97	96.3 ± 3.4	204.8 ± 6.9
	0.06	25.98 ± 0.44	27.50 ± 0.41	12.08 ± 0.30	18.09 ± 0.34	69.31 ± 0.94	99.4 ± 2.6
	0.10	19.07 ± 0.36	20.22 ± 0.34	10.03 ± 0.26	13.57 ± 0.28	41.69 ± 0.77	54.3 ± 1.9
	0.16	13.43 ± 0.21	12.87 ± 0.19	7.88 ± 0.16	8.51 ± 0.15	27.86 ± 0.44	27.98 ± 0.98
	0.24	7.22 ± 0.16	7.13 ± 0.14	5.21 ± 0.13	4.47 ± 0.11	14.79 ± 0.32	8.79 ± 0.55
	0.32	4.18 ± 0.12	3.47 ± 0.10	3.74 ± 0.11	2.510 ± 0.085	8.36 ± 0.24	2.83 ± 0.32
	0.40	2.566 ± 0.097	2.215 ± 0.081	2.534 ± 0.092	1.399 ± 0.063	5.01 ± 0.19	0.62 ± 0.14
	0.48	1.354 ± 0.071	1.119 ± 0.058	1.683 ± 0.076	0.844 ± 0.050	3.10 ± 0.15	0.55 ± 0.14
	0.56	0.807 ± 0.056	0.640 ± 0.046	1.220 ± 0.066	0.413 ± 0.036	1.89 ± 0.12	0.232 ± 0.086
6	0.00	36.6 ± 1.4	41.57 ± 0.99	16.4 ± 1.3	30.25 ± 0.93	93.6 ± 3.3	185.9 ± 6.6
	0.06	24.61 ± 0.42	25.65 ± 0.35	11.41 ± 0.29	17.00 ± 0.40	55.53 ± 0.86	88.0 ± 3.8
	0.10	18.35 ± 0.35	18.15 ± 0.28	9.81 ± 0.26	12.72 ± 0.33	38.00 ± 0.69	55.5 ± 3.0
	0.16	11.91 ± 0.20	11.72 ± 0.16	7.06 ± 0.15	7.94 ± 0.18	24.78 ± 0.40	26.5 ± 1.4
	0.24	6.77 ± 0.15	6.24 ± 0.11	4.96 ± 0.13	4.47 ± 0.14	13.60 ± 0.29	8.26 ± 0.83
	0.32	3.84 ± 0.11	3.511 ± 0.089	3.28 ± 0.11	2.41 ± 0.10	7.06 ± 0.21	2.69 ± 0.45
	0.40	2.190 ± 0.088	1.870 ± 0.065	2.242 ± 0.089	1.265 ± 0.074	4.51 ± 0.17	1.05 ± 0.28
	0.48	1.244 ± 0.067	0.960 ± 0.047	1.564 ± 0.075	0.704 ± 0.056	2.53 ± 0.13	0.20 ± 0.10
	0.56	0.784 ± 0.053	0.594 ± 0.037	1.047 ± 0.062	0.503 ± 0.048	1.55 ± 0.10	0.20 ± 0.10

TABLE X. Results of fitting the cross sections. Fits of the type $A\exp(Bt)$ were made to the $\pi^{\pm}$ and $K^{\pm}$ cross sections for the range $0.05 \leq -t \leq 0.44$ GeV^2; the form $A\exp(Bt+Ct^2)$ was used for p and for $\bar{p}$ data over the intervals 0.05 to 1.0 GeV^2 and 0.05 to 0.44 GeV^2, respectively. The superscripts ± refer to the charge of the incident particle. Errors shown include statistical errors and uncertainty in the corrections for single Coulomb scattering.

Beam	p_{beam} (GeV/c)	A^+ (mb/GeV^2)	B^+ (GeV^{-2})	C^+ (GeV^{-4})	χ^2 per degree of freedom	A^- (mb/GeV^2)	B^- (GeV^{-2})	C^- (GeV^{-4})	χ^2 per degree of freedom
π	3	52.7±1.2	7.03±0.12		17/19	55.6±1.1	7.61±0.11		24/19
	3.65	44.8±1.0	6.75±0.12		20/19	51.5±1.2	7.60±0.12		14/19
	5	39.4±0.7	6.94±0.09		24/19	44.1±0.7	7.66±0.09		32/19
	6	37.1±0.7	7.08±0.10		14/19	40.2±0.6	7.70±0.08		33/19
K	3	17.5±0.4	3.64±0.11		24/19	38.7±0.9	7.96±0.13		16/19
	3.65	17.1±0.5	4.12±0.12		29/19	33.9±0.8	7.57±0.13		22/19
	5	16.2±0.4	4.62±0.10		23/19	28.9±0.6	7.65±0.10		24/19
	6	15.7±0.4	4.87±0.11		12/19	27.0±0.7	7.57±0.13		18/19
p	3	117.0±2.3	7.80±0.15	2.66±0.20	19/26	299±19	12.2±0.8	−5.7±2.4	28/18
	3.65	110.1±2.4	8.29±0.16	3.06±0.22	23/26	264±20	12.1±1.0	−7.6±3.0	12/18
	5	97.3±2.0	8.46±0.16	2.66±0.22	22/26	194±14	11.4±1.0	−5.9±2.9	15/18
	6	91.2±1.9	8.63±0.16	2.50±0.23	31/26	198±22	12.4±1.5	−2.5±4.0	19/18

while in better agreement than their early results,[6] still tend to be somewhat lower than this experiment. However, this discrepancy depends on the reaction and the momentum transfer region.

The spread in previous data emphasizes the need for the systematic survey of the present experiment. The general agreement of the data from this and previous experiments is additional evidence that there are no large systematic errors in the data presented here.

E. Total elastic scattering cross sections

The total elastic scattering cross sections at each of the four beam momenta are listed in Table XI and compared with previous results[41] in Fig. 6. These values were obtained by integrating the fits of Table X from $-t=0$ to 0.44 GeV^2, and then numerically integrating the experimental values of $d\sigma/dt$ from 0.44 maximum t of this experiment, about 2 GeV^2. Corrections for the contribution at larger t were made using estimates derived from previously published work. This correction ranged from typically 2% at 3 GeV/c to 0.2% at 6 GeV/c.

F. Slope at $t=0$

The $t=0$ slopes of our cross sections (parameter B in Table X) are compared in Fig. 7 with previous values (obtained from the compilation of Lasinski *et al.*[42]). Generally, the results of this experiment are in good agreement with previous results, although the old values show considerable fluctuation, especially for pp and $\bar{p}p$, where linear fits have often been made in the past. The results of Foley *et al.*[30,43] for $\pi^{\pm}$ at $p_{\text{lab}} \gtrsim 7$ GeV/c do not join smoothly onto the lower-energy results, as has been noted previously.[37,44] Our values for the pp quadratic coefficient are shown in Fig. 8; they agree well with those found previously[43,45-47] and show little variation with momentum.

The energy dependence of the forward slopes was determined by fits of the type

$$B = B_0 + B' \ln\left(\frac{p_{\text{lab}}}{4\ \text{GeV}/c}\right), \tag{11}$$

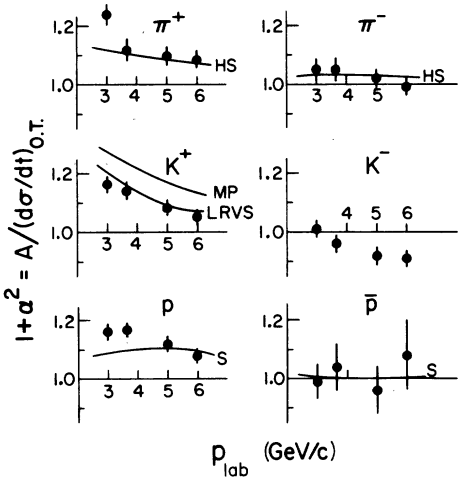

FIG. 4. The quantity $1+\alpha^2 = A/(d\sigma/dt)_{\text{O.T.}}$ plotted vs laboratory momentum for the six particles indicated. α is the real-to-imaginary ratio, A is the $t=0$ cross section found from the fits of Table X, and $(d\sigma/dt)_{\text{O.T.}}$ is the optical-theorem cross section. The curves shown are from calculations of Höhler and Strauss (HS) (Ref. 31), Martin and Poole (MP) (Ref. 39), Lusignoli *et al.*, (LRVS) (Ref. 32), and Söding (S) (Ref. 35).

with results given in Table XII. The coefficient B' is twice the slope of the effective Regge trajectory. The energy dependence of the quadratic coefficient C is also shown for pp and $\bar{p}p$ scattering. The fits are all quite reasonable, the worst χ^2 probability being 15%. The $\pi^\pm$ and $\bar{p}$ slopes are constant to within one standard deviation; the K^- data show marginal antishrinkage (1.7 standard deviations), while the K^+ and proton data show a very definite shrinking.

Leader and Pennington[48] suggested that a new variable be used in place of t and that the use of this variable would reduce the energy dependence of the slope and hasten the approach to asymptopia, especially for K^+ and proton elastic scattering. Their parameter reduces to

$$-n^2 = \left(\frac{2Mp_{\text{lab}}}{s}\right)^2 p_T^{\,2}, \tag{12}$$

where M is the proton mass, s is the center-of-mass energy squared, and p_T is the transverse momentum of the scattered particle. If one fits the small-t data to the form $e^{\beta n^2}$ instead of e^{Bt}, then

$$\beta \approx \frac{B}{(2Mp_{\text{lab}}/s)^2}. \tag{13}$$

Values of β have been calculated from the B's of Table X and tested for energy dependence by taking the difference between the values at 3 and 6 GeV/c. The results are shown in Table XIII. For comparison, differences of the parameter B are also shown. While only K^+ and proton slopes, as represented by the parameter B, show significant dependence, all β's show considerable variation from 3 to 6 GeV/c. Thus the description of our small-t data is simpler in terms of t than in terms of the Leader-Pennington variable n^2.

The slopes of our forward peaks agree qualitatively with a simple geometric model of Krisch.[49] In this model, two Lorentz-contracted Gaussian distributions are folded together to predict the forward slope for xp elastic scattering to be

$$B_{xp}(s) = \tfrac{1}{2}(A_x^{\,2}\beta_x^{\,2} + A_p^{\,2}\beta_p^{\,2}) \frac{\sigma_{\text{tot}}^{xp}(s)}{\sigma_{\text{tot}}^{xp}(s=\infty)} \tag{14}$$

In this equation β_x is the center-of-mass velocity of the interacting particle (pion, kaon, or proton) and β_p is the velocity of the target proton. The symbol $\sigma_{\text{tot}}^{xp}(s)$ denotes the total xp cross section at center-of-mass energy $\sqrt{s}$. The $A_x^{\,2}$ are the only free parameters and are related to the effective rms radius of a particle at high energy by

$$\langle R_x^{\,2}\rangle_{s=\infty} = \tfrac{3}{2}A_x^{\,2}. \tag{15}$$

Variation of radii with energy is assumed to be given by

$$\sigma_{\text{tot}} \propto R^2. \tag{16}$$

The curves in Fig. 7 show the results of this model

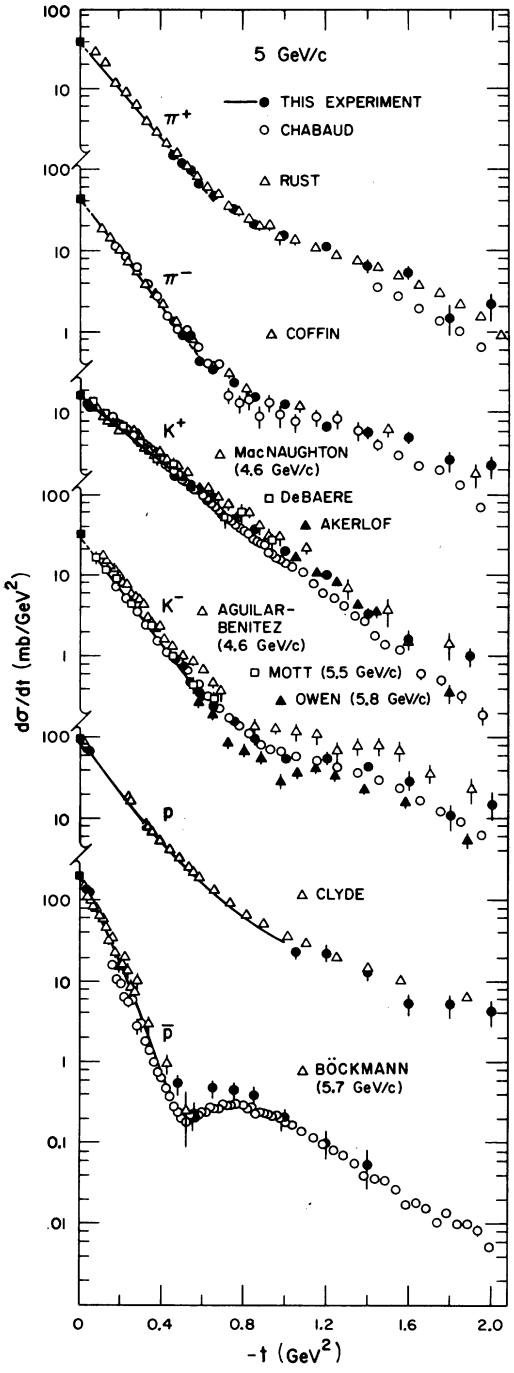

FIG. 5. Comparison with other experiments (Refs. 7–17) at beam momentum 5 GeV/c (or as labeled). For clarity the results of this experiment are shown as solid lines corresponding to the fits of Table X in the t interval used for the fits.

TABLE XI. Total elastic cross sections. The errors shown are dominated by the over-all normalization uncertainty of ±4%; the particle-antiparticle relative uncertainty (including statistics) is about ±2.3% for $\pi^{\pm}$ and $K^{\pm}$ and ±3% for p and $\bar{p}$.

p (GeV/c)	$\sigma(\pi^+p)$ (mb)	$\sigma(\pi^-p)$ (mb)	$\sigma(K^+p)$ (mb)	$\sigma(K^-p)$ (mb)	$\sigma(pp)$ (mb)	$\sigma(\bar{p}p)$ (mb)
3	7.84 ± 0.33	7.57 ± 0.31	4.81 ± 0.20	5.06 ± 0.21	17.2 ± 0.7	23.7 ± 1.0
3.65	6.88 ± 0.29	6.97 ± 0.29	4.26 ± 0.18	4.60 ± 0.19	15.2 ± 0.6	20.6 ± 0.9
5	5.79 ± 0.24	5.85 ± 0.24	3.53 ± 0.15	3.84 ± 0.16	12.7 ± 0.5	16.0 ± 0.7
6	5.33 ± 0.22	5.30 ± 0.22	3.26 ± 0.14	3.62 ± 0.15	11.5 ± 0.5	15.6 ± 0.8

for $A^2 = 6$, 3, and 10.5 GeV^{-2} for π, K, and proton, respectively. These values, whose determination is described below, correspond to rms radii of 0.59, 0.42, and 0.78 F. With only three parameters the model of Krisch qualitatively describes the slopes down to about 2 GeV/c.

The slopes at each of our four momenta were used to separately calculate the A's of Krisch's model. For protons and antiprotons the slope of the quadratic fits at $-t = 0.10$ GeV^2 was used, this being a typical momentum transfer for the forward peak. The $A_p{}^2$'s obtained are shown in Fig. 9 and, as expected, seem fairly independent of incident momentum. The values found with the $\bar{p}p$ slopes are somewhat higher, but this depends on the t value at which the slope is evaluated. Taking $A_p{}^2 = 10.5$ GeV^{-2}, $A_{\pi^{\pm}}{}^2$ and $A_{K^{\pm}}{}^2$ were calculated. As expected, $A_{\pi^+}{}^2 \approx A_{\pi^-}{}^2$ and there is little variation with energy. While $A_{K^+}{}^2$ is also energy-independent, $A_{K^-}{}^2$ varies considerably, going from 5.1 to 3.4 GeV^{-2} from 3 to 6 GeV/c. Although the agreement of $A_{K^-}{}^2$ with $A_{K^+}{}^2$ improves with increasing energy, a difference of 1.1 ± 0.3 GeV^{-2} still remains at 6 GeV/c.

G. Shape of the diffraction peak

The question of the exact shape of the forward elastic scattering peak has received considerable attention recently with the observation[50] at the CERN ISR of a fairly sharp change of slope in pp elastic scattering near $-t = 0.1$ GeV^2. Similar effects had been noted previously for protons at lower energies by Carrigan,[51] and it has been recently suggested that they may also be present in πp scattering at small t.[37] In an effort to find deviations from the exponential fits of Table X, we

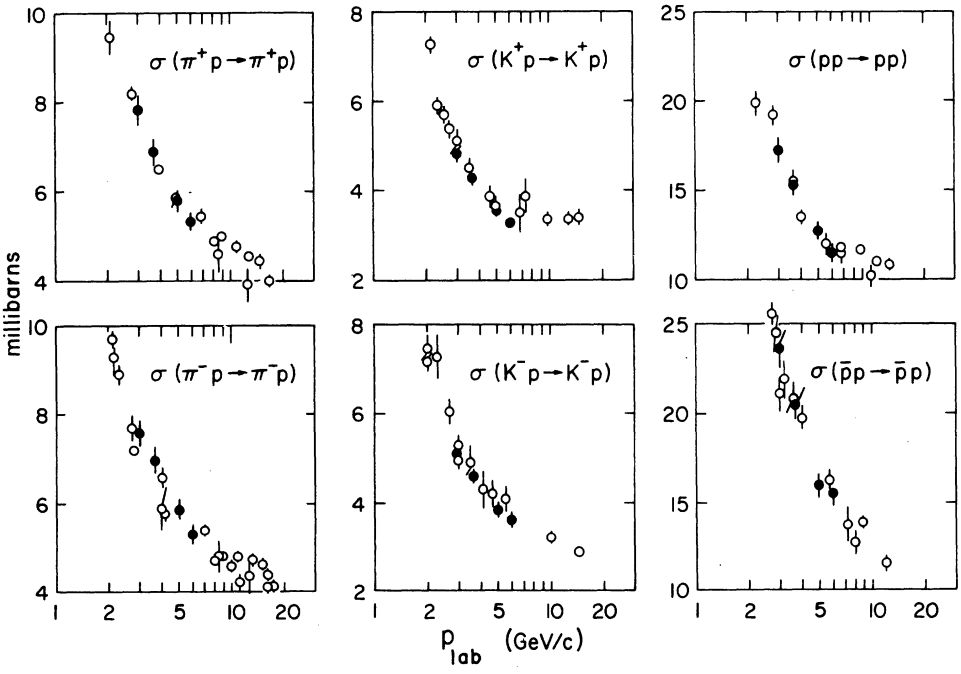

FIG. 6. Comparison of the total elastic scattering cross sections of this experiment (solid points) with previous results (Ref. 41); see Table XI for a discussion of the errors.

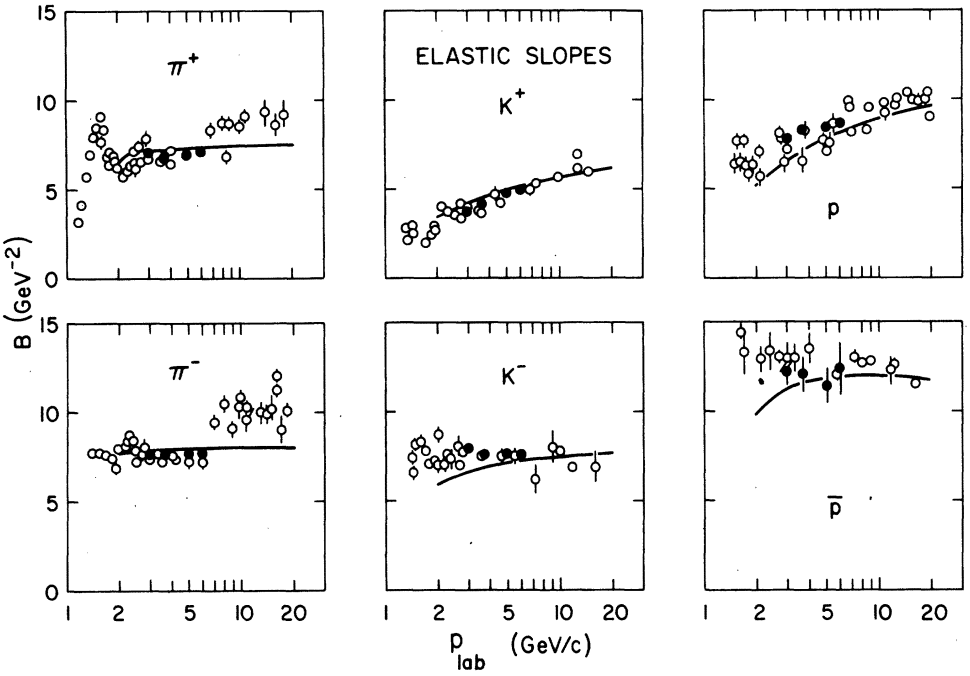

FIG. 7. Comparison of the $t = 0$ slopes of the differential cross sections of this experiment (solid points) with previous experimental results from the compilation of Lasinski *et al.* (Ref. 42). The curves are from the geometric model of Krisch (Ref. 49).

have plotted in Fig. 10 the ratio of data values to the fitted values, together with the statistical uncertainty in the fitted function. Although it is possible to find deviations at any one energy, none has high statistical significance nor is present at other momenta.

To estimate the sensitivity of the results to the form used, fits were also made using the sum of two exponentials

$$\frac{d\sigma}{dt} = a_1 e^{b_1 t} + a_2 e^{b_2 t} \tag{17}$$

over the interval $0 \leq -t < 1.5$ GeV^2. The results are shown in Table XIV. The $\pi^\pm$ and $K^\pm$ fits were only qualitatively successful, with the χ^2 per degree of freedom averaging 1.26. The $\bar{p}$ fits were not at all good, as one might expect from a simple inspection of Fig. 3.

The proton fits were excellent, with a total χ^2 of 123 for 132 degrees of freedom. The fitted function follows the quadratic fit of Eq. (8) and Table X to within ±3% from $-t = 0$ to 0.7 GeV^2 (±10% to 1.3 GeV^2), and there is little basis on which to choose between the two forms. The two-exponential fits at 3 and 3.65 GeV/c extrapolate somewhat better to the values expected at $t = 0$, while the 6-GeV/c fit is a little worse.

The $t = 0$ slope for the two-exponential fit is given by

$$B = (a_1 b_1 + a_2 b_2)/(a_1 + a_2) .$$

For $\pi^\pm$ and $K^\pm$ these slopes are very close to those of the linear fits. The $t = 0$ proton slopes from the two-exponential fits are definitely smaller, by about 0.6 GeV^{-2}, an indication of the systematic uncertainty involved in the determination of this quantity.

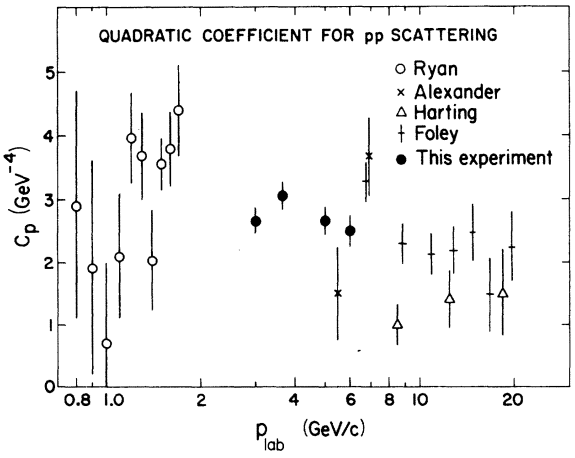

FIG. 8. Comparison of the quadratic coefficients from the pp fits of this experiment and that of previous experiments (Refs. 43, 45–47).

TABLE XII. Momentum dependence of the forward slopes B and quadratic coefficients C of Table X. Fits were made to the form $B = B_0 + B' \ln(p_{\text{lab}}/4\ \text{GeV}/c)$; the χ^2 goodness of fit is shown for 2 degrees of freedom.

Particle	B_0 (GeV^{-2})	B' (GeV^{-2})	χ^2	C_0 (GeV^{-4})	C' (GeV^{-4})	χ^2
π^+	6.94 ± 0.06	0.18 ± 0.20	4.1			
π^-	7.64 ± 0.05	0.14 ± 0.18	0.1			
K^+	4.20 ± 0.06	1.76 ± 0.20	0.9			
K^-	7.72 ± 0.06	−0.42 ± 0.24	3.0			
p	8.22 ± 0.08	1.11 ± 0.29	1.7	2.74 ± 0.11	−0.35 ± 0.40	2.7
$\bar{p}$	12.0 ± 0.5	−0.6 ± 2.0	0.4	−5.7 ± 1.5	3 ± 6	0.8

H. $C=+1$ exchange

The average of particle and antiparticle cross sections

$$\Sigma = \tfrac{1}{2}\left[\frac{d\sigma}{dt}(x^- p) + \frac{d\sigma}{dt}(x^+ p)\right] \tag{18}$$

is shown in Fig. 11 for 5 GeV/c. Here $x^{\pm}$ indicates the beam particle. Interference between the amplitudes F^+ and F^-, corresponding to t-channel exchange with charge conjugation $C=+1$ and -1, is eliminated by this average:

$$\Sigma = |F^+|^2 + |F^-|^2 \tag{19}$$

(the sum over nucleon spins has been omitted for clarity). One usually assumes the dominance of F^+, in which case

$$\Sigma \approx |F^+|^2 . \tag{20}$$

The Pomeron dominates the F^+ amplitude, but at our energies Pomeron interference with f exchange is also important[52,53]:

$$\Sigma \approx |P + f|^2_{\text{nonflip}} . \tag{21}$$

A minimum amount of F^- is required by the particle-antiparticle cross-section differences,

$$\left|\frac{F^-}{F^+}\right| \geq \frac{|[d\sigma/dt(x^- p)]^{1/2} - [d\sigma/dt(x^+ p)]^{1/2}|}{[d\sigma/dt(x^- p)]^{1/2} + [d\sigma/dt(x^+ p)]^{1/2}} . \tag{22}$$

The equal sign would hold if F^- and F^+ were in phase and populated the same spin state. This minimum value is shown in Fig. 12 for 5 GeV/c. At intermediate momentum transfer $|F^-/F^+|$ must be at least 10% for kaons and 20% for protons.

Exponential fits to Σ were made over the range $0.05 < -t < 0.44$ GeV^2, with results shown in Table XV. Although the linear form follows the pion data out to $-t \approx 0.7$ GeV^2, the kaon and proton fits worsen considerably when the range is extended from 0.44 to 0.70 GeV^2. Fits to the sum of two

TABLE XIII. Differences of the forward 3- and 6-GeV/c slopes for the forms e^{Bt} and $e^{\beta n^2}$, where n^2 is the Leader-Pennington variable (Ref. 48).

Particle	$B_6 - B_3$ (GeV^{-2})	$\beta_6 - \beta_3$ (GeV^{-2})
π^+	0.05 ± 0.16	−1.20 ± 0.20
π^-	0.09 ± 0.14	−1.26 ± 0.17
K^+	1.23 ± 0.16	0.60 ± 0.21
K^-	−0.39 ± 0.18	−2.45 ± 0.25
p	0.83 ± 0.22	−2.78 ± 0.35
$\bar{p}$	0.2 ± 1.7	−5.8 ± 2.6

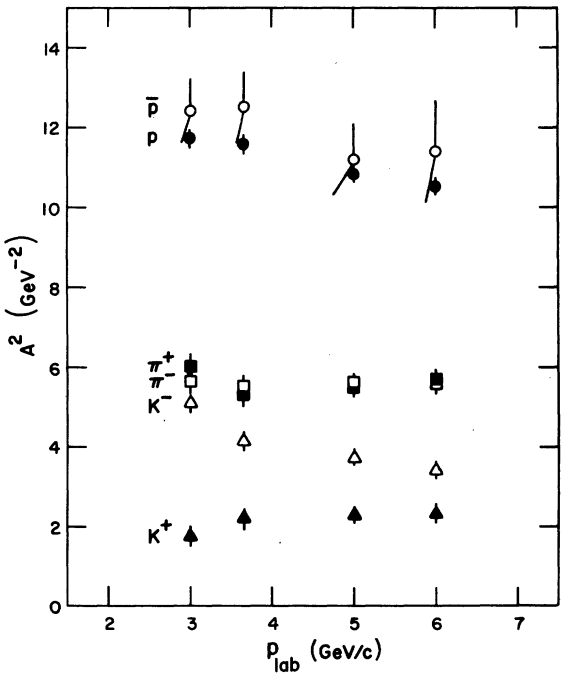

FIG. 9. The radius parameters A^2 calculated from the data of this experiment for the geometric model of Krisch (Ref. 49).

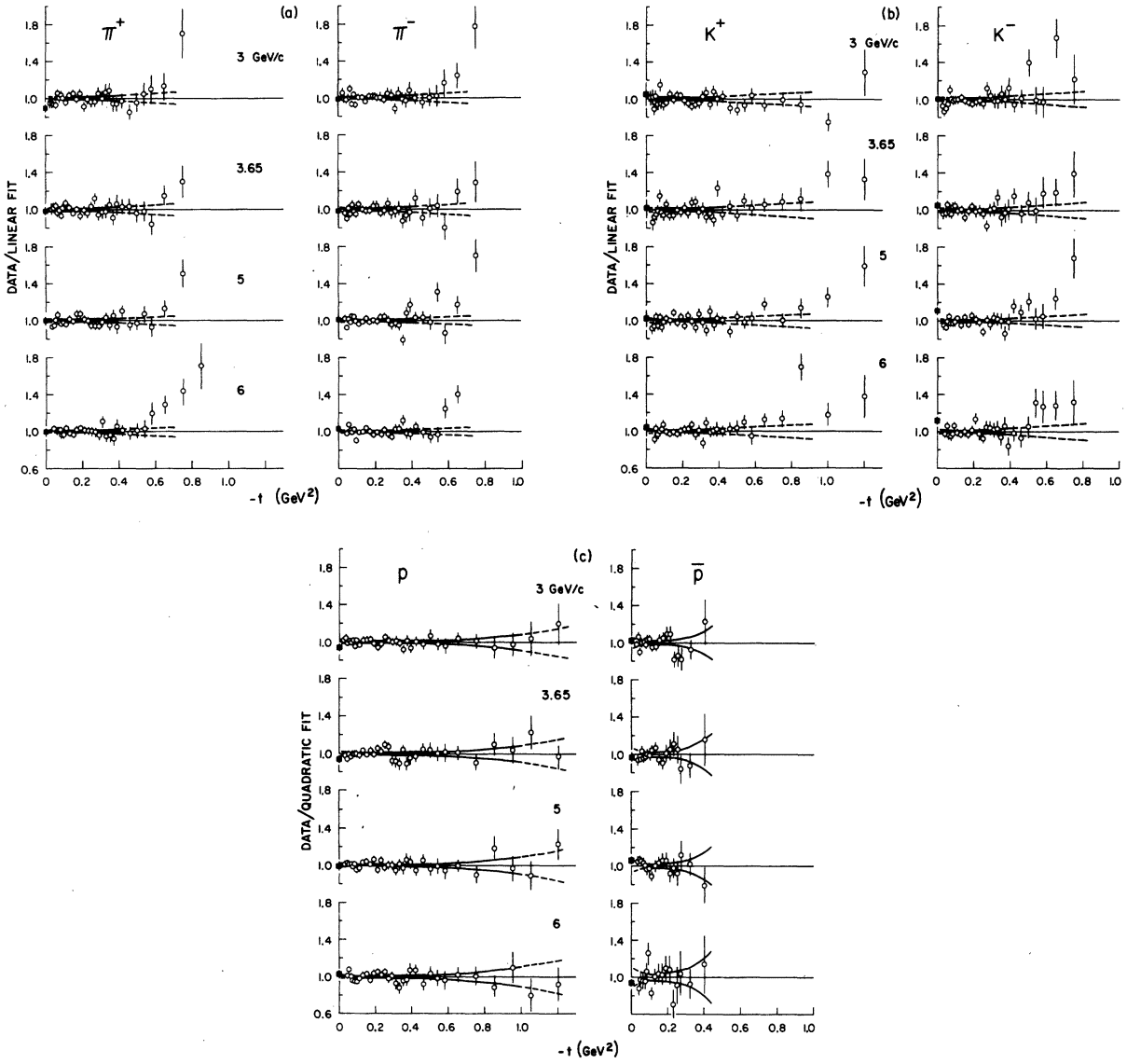

FIG. 10. Ratio of the experimental cross sections and the exponential fits of Table X. The square points at $t = 0$ were derived from total cross section and real-to-imaginary ratio via the optical theorem. The curves show the statistical uncertainty in the fitted function and are dashed beyond the t region used in the fits: (a) pion comparison, (b) kaon comparison, and (c) proton comparison.

exponentials were made over the interval 0 to 1.5 GeV^2, with results shown in Table XVI. Good fits were found for Σ_p, but several of the π and K fits had rather large χ^2. The 5-GeV/c fits to two exponentials are compared with the data in Fig. 11.

I. The crossover point

The crossover point t_c is defined as that value of momentum transfer for which particle and antiparticle have equal cross sections. As has been known for some time, all three particles have crossovers in the neighborhood of 0.2 GeV^2. To determine the crossover from our data, we fit

$$\ln\left[\frac{d\sigma}{dt}(x^- p)\Big/\frac{d\sigma}{dt}(x^+ p)\right] = a + bt \tag{23}$$

over the interval $0.05 < -t < 0.28$ GeV^2 for $\pi^\pm$ and $K^\pm$. For protons, the more restricted range 0.08–0.22 GeV^2 was used to reduce the effect of curvature and a correction of 0.002 GeV^2 was made to compensate for this systematic effect. The crossover points, given by

TABLE XIV. Results of fits to the differential cross sections over the range $0 \le -t < 1.5$ GeV^2 using the sum of two exponentials, $d\sigma/dt = a_1 e^{b_1 t} + a_2 e^{b_2 t}$. A and B are the corresponding $t = 0$ intercept and effective slope. Fits of this type failed for the $\bar{p}$ data, and their results are not given here.

	p (GeV/c)	a_1 (mb/GeV^2)	b_1 (GeV^{-2})	a_2 (mb/GeV^2)	b_2 (GeV^{-2})	A (mb/GeV^2)	B (GeV^{-2})	χ^2 per degree of freedom
π^+	3	51.8 ± 0.9	7.17 ± 0.14	0.27 ± 0.20	0.43 ± 0.70	52.1 ± 1.0	7.14 ± 0.12	49/34
	3.65	45.6 ± 0.8	7.04 ± 0.14	0.28 ± 0.16	0.56 ± 0.47	45.9 ± 0.9	7.00 ± 0.12	42/33
	5	39.4 ± 0.6	7.14 ± 0.10	0.25 ± 0.10	0.85 ± 0.38	39.6 ± 0.6	7.10 ± 0.09	40/33
	6	37.5 ± 0.6	7.33 ± 0.13	0.37 ± 0.18	1.50 ± 0.4	37.9 ± 0.6	7.28 ± 0.11	22/32
π^-	3	56.0 ± 0.9	7.80 ± 0.11	0.21 ± 0.11	0.31 ± 0.50	56.2 ± 0.9	7.77 ± 0.10	42/34
	3.65	51.4 ± 0.9	7.73 ± 0.10	0.06 ± 0.03	−0.81 ± 0.43	51.4 ± 0.9	7.72 ± 0.10	38/33
	5	44.3 ± 0.6	7.88 ± 0.10	0.23 ± 0.09	0.98 ± 0.34	44.5 ± 0.6	7.84 ± 0.09	62/33
	6	40.7 ± 0.5	8.03 ± 0.11	0.42 ± 0.14	1.64 ± 0.32	41.1 ± 0.6	7.96 ± 0.10	51/32
K^+	3	18.1 ± 2.0	3.64 ± 0.23	−0.6 ± 2.2	2.2 ± 2.0	17.48 ± 0.37	3.69 ± 0.12	41/33
	3.65	15.8 ± 2.2	4.10 ± 0.26	0.8 ± 2.3	2.7 ± 2.0	16.58 ± 0.38	4.03 ± 0.14	43/33
	5	15.1 ± 2.0	4.77 ± 0.34	0.9 ± 2.1	2.7 ± 1.5	16.00 ± 0.33	4.66 ± 0.13	44/33
	6	14.0 ± 3.0	5.09 ± 0.48	1.6 ± 3.2	3.1 ± 1.8	15.52 ± 0.37	4.89 ± 0.21	34/29
K^-	3	37.6 ± 0.7	7.88 ± 0.11	0.03 ± 0.03	−0.8 ± 0.7	37.61 ± 0.67	7.87 ± 0.11	39/34
	3.65	34.2 ± 0.7	7.76 ± 0.13	0.12 ± 0.07	0.7 ± 0.6	34.33 ± 0.69	7.73 ± 0.12	37/33
	5	28.7 ± 0.5	7.69 ± 0.10	0.06 ± 0.03	0.2 ± 0.5	28.78 ± 0.47	7.68 ± 0.09	44/33
	6	27.5 ± 0.6	7.83 ± 0.16	0.17 ± 0.11	1.2 ± 0.5	27.70 ± 0.60	7.79 ± 0.14	30/32
p	3	107.3 ± 1.9	7.64 ± 0.23	6.6 ± 2.1	2.2 ± 0.3	113.9 ± 1.9	7.32 ± 0.15	31/34
	3.65	99.9 ± 1.7	7.76 ± 0.20	4.1 ± 1.1	1.9 ± 0.3	104.0 ± 1.9	7.53 ± 0.15	25/33
	5	90.5 ± 1.4	8.04 ± 0.18	3.4 ± 1.1	2.4 ± 0.3	93.9 ± 1.6	7.84 ± 0.14	29/33
	6	83.1 ± 1.9	8.55 ± 0.27	6.0 ± 2.2	3.5 ± 0.4	89.1 ± 1.7	8.21 ± 0.17	38/32

$$-t_c = a/b\,, \tag{24}$$

are listed in Table XVII and displayed in Fig. 13, with statistical errors indicated. The systematic errors in t_c are ±0.025, ±0.004, and ±0.002 GeV^2 for pion, kaon, and proton, respectively, corresponding to the 1.5% uncertainty in relative normalization.

The crossover points are consistent with no energy dependence, as seen in Fig. 13 and by fits to

$$t_c = t_0 + t' \ln\left(\frac{p_{\text{lab}}}{4\ \text{GeV}/c}\right). \tag{25}$$

The most suggestive case (that for kaons) yields a value for t' one standard deviation from zero, implying a change in $-t_c$ of 0.010 ± 0.010 GeV^2 for the factor-of-2 change in beam momentum from 3 to 6 GeV/c. For the pion and proton cases the corresponding change is −0.017 ± 0.032 and −0.003 ± 0.008 GeV^2, respectively. Our pion crossover points connect within errors to the finite-energy-sum-rule result[54] $-t_c = 0.25 \pm 0.10$ GeV^2 at 1.5 GeV/c. Energy independence of the kaon crossover is also suggested by the preliminary result of a recent 13-GeV/c SLAC measurement,[55] 0.22 ± 0.03 GeV^2, within errors of our average value of 0.190 ± 0.006 GeV^2.

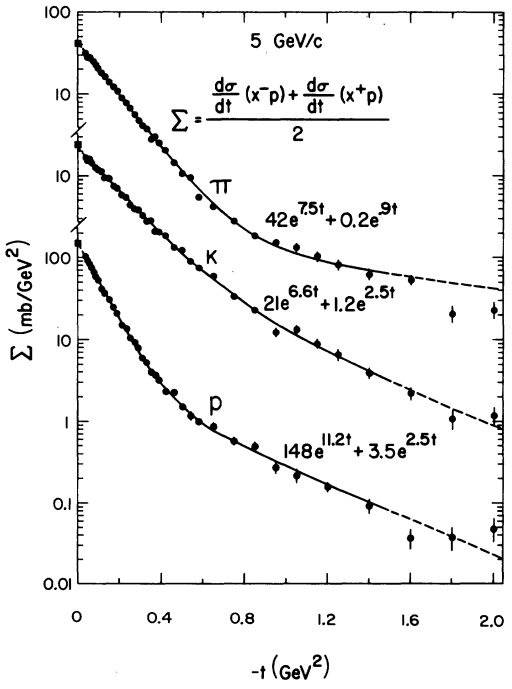

FIG. 11. Average of the particle-antiparticle cross sections at 5 GeV/c. The curves show results of fits over the range 0–1.5 GeV^2 using the sum of two exponentials (Table XVI).

Equating the first zero of $J_0(r(-t)^{1/2})$ with the crossover point, one can calculate the effective radius for the source of the $C=-1$ amplitude:

$$r = 0.475/(-t_c)^{1/2}\ \text{F} \tag{26}$$

for t_c in GeV^2. The average values of t_c and the corresponding radii are listed in Fig. 13; the errors include systematic uncertainties. The kaon crossover points are displaced 0.028 ± 0.007 GeV^2 from the proton crossovers, giving an effective radius of 1.09 F instead of 1.18 F. While compatible with the proton, the radius for πp scattering may be somewhat larger. The fact that $-t_c$ for kaons is slightly larger than for pions has been ascribed in part to a difference in absolute phase for the nonflip $I_t=0$ amplitude and in part to the $\pi\pi$ high partial-wave contribution.[56]

Since t_c is energy-independent, the effective radii are also energy-independent, as expected in simple geometric models. This disagrees with the geometric model of Krisch,[49] described above, for which $r^2 \propto \sigma_{\text{tot}}$. For pp and $\bar{p}p$ interactions such a dependence would change r by factors of 0.96 and 0.88, respectively, when going from 3 to 6 GeV/c, compared with the factor calculated from Eq. (26) of 1.01 ± 0.02. Apparently the sources for F^+ and F^- are independent, the diffractive radius changing with energy and particle while the effective source radius of the $C=-1$ amplitude remains fixed. This result casts doubt on the strong-absorption idea that the source of F^- is the periphery of the strongly absorbing region, in which case the radii for F^- and F^+ should scale together.

The energy independence of our results also disagrees with the suggestion of Cline and Matos[57] that the K crossover moves as $-t_c = 0.35 p_{\text{lab}}^{-0.48}$

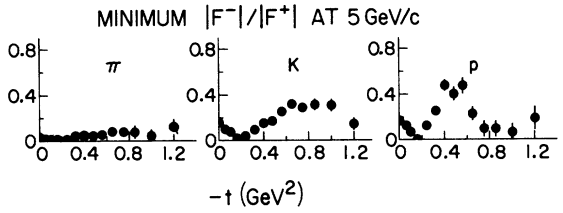

FIG. 12. Minimum value of the ratio $|F^-|/|F^+|$ of the amplitudes for t-channel exchange with $C=-1$ and $+1$ at 5 GeV/c.

GeV^2, a change of -0.06 GeV^2 going from 3 to 6 GeV^2 compared with our $+0.01 \pm 0.01$ GeV^2. Although the errors are relatively large, the pion crossover does not appear to move out with increasing energy as suggested by Hartley and Kane.[58] Our values for the crossovers are in disagreement with the results of various calculations; for example, Park *et al.*[59] found a pion crossover of 0.26 GeV^2 at 6 GeV/c in a complex-Regge-pole model, and Henzi *et al.*[60] calculated a kaon crossover of 0.3 GeV^2 at 5 GeV/c in a Regge eikonal model.

J. $C=-1$ exchange

The quantity

$$\Delta = \frac{\sigma^- - \sigma^+}{[8(\sigma^- + \sigma^+)]^{1/2}} \tag{27}$$

is plotted in Fig. 14, where $\sigma^\pm \equiv d\sigma/dt(x^\pm p)$. This quantity should, to a good approximation, isolate that part of the $C=-1$ exchange amplitude with the same phase and spin state as the $C=+1$ amplitude, expected to be mainly imaginary nonflip.[61] The errors shown are mainly statistical, with the $t=0$

TABLE XV. Polynomial fits to $\ln[\frac{1}{2}(d\sigma^+/dt + d\sigma^-/dt)]$ over the interval $0.05 < -t < 0.44$ GeV^2, similar to the fits of Table X.

	p (GeV/c)	A (mb/GeV^2)	B (GeV^{-2})	C (GeV^{-4})	χ^2 per degree of freedom
Σ_π	3	54.0 ± 0.8	7.31 ± 0.08		23/19
	3.65	48.0 ± 0.8	7.16 ± 0.08		23/19
	5	41.7 ± 0.5	7.30 ± 0.06		25/19
	6	38.6 ± 0.4	7.39 ± 0.06		20/19
Σ_K	3	25.9 ± 0.4	5.65 ± 0.08		30/19
	3.65	24.3 ± 0.4	5.80 ± 0.09		24/19
	5	21.7 ± 0.3	6.09 ± 0.07		31/19
	6	20.7 ± 0.4	6.20 ± 0.09		18/19
Σ_p	3	225 ± 7	12.5 ± 0.4	6.6 ± 0.9	21/18
	3.65	200 ± 8	12.4 ± 0.4	5.5 ± 1.0	18/18
	5	152 ± 6	11.3 ± 0.4	3.4 ± 1.0	18/18
	6	153 ± 9	12.2 ± 0.6	5.2 ± 1.5	20/18

TABLE XVI. Fits to $\Sigma = \frac{1}{2}[d\sigma/dt\,(x^-p) + d\sigma/dt\,(x^+p)]$ over the range $0 \le -t < 1.5$ GeV^2 using the sum of two exponentials, $a_1 e^{b_1 t} + a_2 e^{b_2 t}$. A and B are the corresponding $t = 0$ intercept and effective slope.

	p (GeV/c)	a_1 (mb/GeV^2)	b_1 (GeV^{-2})	a_2 (mb/GeV^2)	b_2 (GeV^{-2})	A (mb/GeV^2)	B (GeV^{-2})	χ^2 per degree of freedom
π	3	54.0 ± 0.6	7.48 ± 0.09	0.22 ± 0.10	0.27 ± 0.43	54.2 ± 0.7	7.45 ± 0.08	62/34
	3.65	48.5 ± 0.6	7.37 ± 0.08	0.14 ± 0.05	−0.13 ± 0.31	48.6 ± 0.7	7.35 ± 0.08	56/33
	5	41.7 ± 0.4	7.49 ± 0.07	0.24 ± 0.07	0.88 ± 0.26	42.0 ± 0.4	7.46 ± 0.07	57/33
	6	39.0 ± 0.4	7.68 ± 0.09	0.42 ± 0.12	1.60 ± 0.26	39.5 ± 0.4	7.62 ± 0.08	31/32
K	3	22.8 ± 1.6	6.79 ± 0.44	4.1 ± 1.9	2.9 ± 0.5	26.9 ± 0.5	6.19 ± 0.19	40/33
	3.65	21.5 ± 1.1	7.02 ± 0.39	3.9 ± 1.3	3.0 ± 0.3	25.4 ± 0.5	6.40 ± 0.19	33/33
	5	20.8 ± 0.4	6.59 ± 0.19	1.3 ± 0.5	2.5 ± 0.3	22.0 ± 0.3	6.35 ± 0.12	53/33
	6	18.9 ± 0.9	7.12 ± 0.34	2.6 ± 1.1	3.3 ± 0.4	21.5 ± 0.4	6.66 ± 0.17	39/32
p	3	204 ± 3	11.7 ± 0.2	6.1 ± 0.8	2.2 ± 0.2	210 ± 4	11.41 ± 0.16	37/33
	3.65	182 ± 3	11.7 ± 0.2	4.3 ± 0.5	2.1 ± 0.2	187 ± 4	11.44 ± 0.17	30/33
	5	148 ± 3	11.2 ± 0.2	3.5 ± 0.6	2.5 ± 0.2	151 ± 3	11.04 ± 0.17	33/32
	6	136 ± 4	11.1 ± 0.2	2.7 ± 0.7	2.8 ± 0.3	139 ± 4	10.92 ± 0.22	26/31

errors enlarged to reflect the uncertainties in relative normalization. The values for Δ_π are considerably smaller than for Δ_K and Δ_p. The key to this difference presumably lies in the fact that G parity forbids ω exchange in pion scattering and that nonflip ω exchange is considerably larger than nonflip ρ exchange.

The curves in Fig. 14 are fits to the form used by Davier and Harari,[1]

$$\Delta = ae^{bt} J_0(r(-t)^{1/2}), \tag{28}$$

over the interval $0 \le -t < 0.8$ GeV^2. This form is appropriate if the imaginary nonflip amplitude is strongly absorbed.[1,62] The fit results are given in Table XVIII. The χ^2's obtained at 3 GeV/c were somewhat large, but otherwise the fits are generally good in this t interval. The values of $a = \Delta(t = 0)$ from the pion fits are somewhat lower than expected; although this discrepancy can be explained by normalization uncertainties, it could be indicative of an even faster rise in Δ_π at small t than given by J_0.[63]

At larger t the fitted function recrosses the abscissa, predicting a second crossover point at $t_c' = 5.3 t_c$. Contrary to this, the data gradually approach zero, becoming rather small, possibly with a second crossover at larger t, but certainly with a much smaller overshoot than predicted. This behavior is consistent with the πN absorption model of Masuda.[64] Also, such discrepancies are not unexpected since real parts and flip amplitudes may be important at these large values of t.

The exponential coefficient b is related to the width of the peak in impact-parameter space.[1] The values found for b by the fits are small for both pions and kaons, consistent with zero within the large errors for pions, but with a systematic energy dependence for the kaons. Some of the

TABLE XVII. Crossover points $-t_c$ (GeV^2) obtained from linear fits on the semilog plot, $\ln(\sigma^-/\sigma^+)$ vs t. The relative normalization uncertainty of ±1.5% is not included in the errors shown.

p_{beam} (GeV/c)	π	K	p
3	0.094 ± 0.040	0.186 ± 0.006	0.169 ± 0.005
3.65	0.166 ± 0.023	0.189 ± 0.006	0.157 ± 0.004
5	0.158 ± 0.022	0.189 ± 0.007	0.159 ± 0.006
6	0.125 ± 0.016	0.202 ± 0.010	0.172 ± 0.010

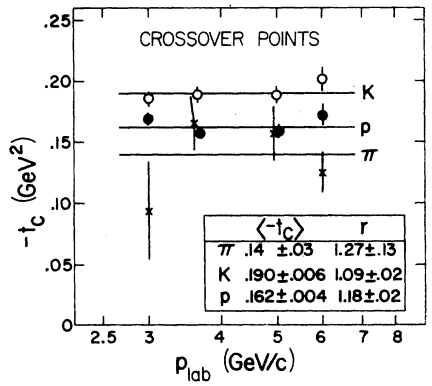

FIG. 13. Comparison of the crossover points t_c for pions, kaons, and protons. The effective radius r (in fermis) was calculated by taking the position of the first zero of $J_0(r(-t)^{1/2})$ at $t = \langle t_c \rangle$. The errors on the plotted points show only the statistical uncertainty, while those for $\langle -t_c \rangle$ and r reflect both the statistical and the ±1.5% uncertainty in the relative particle-antiparticle normalization.

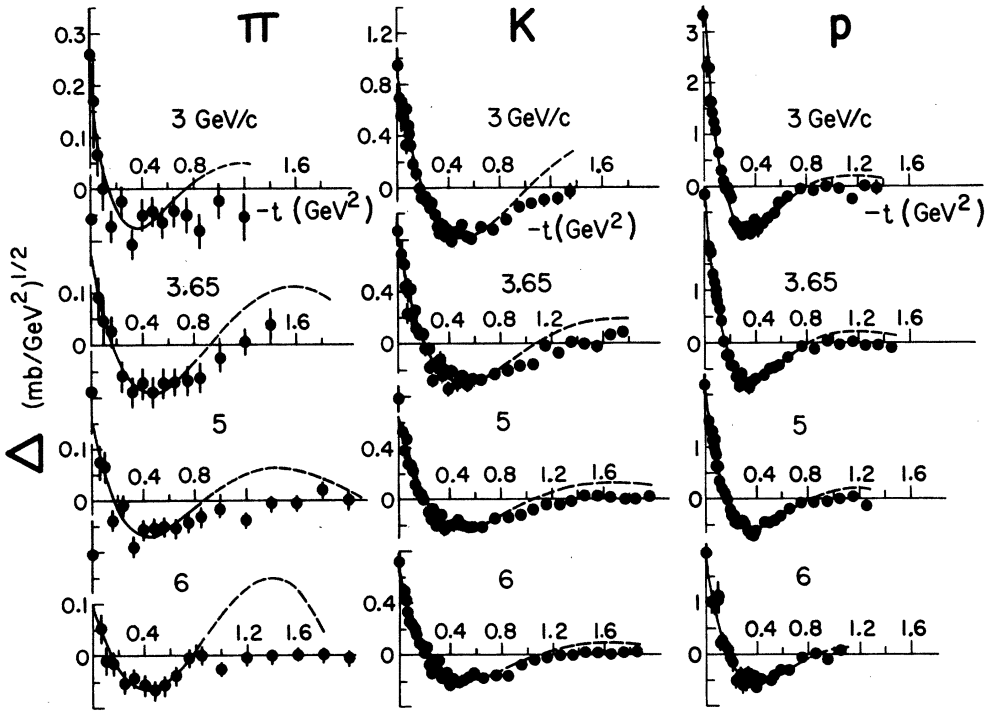

FIG. 14. Fits to the quantity $\Delta = (\sigma^- - \sigma^+)/[8(\sigma^- + \sigma^+)]^{1/2}$ with a parameterization of the form $ae^{bt}J_0(r(-t)^{1/2})$ over the interval $0 \leq -t < 0.8$ GeV^2 as suggested by Davier and Harari (Ref. 1). These fits are summarized in Table XVIII.

pion and kaon fits give unphysical values of b, less than zero, but always consistent with zero. For protons $b \approx 1$ GeV^{-2} and slowly decreases with momentum. The parameter r is mainly determined by the crossover point and therefore has the energy independence discussed previously.

For their amplitude analysis, Halzen and Michael estimated the elastic-scattering differential cross sections by interpolating the existing data.[2] Our data agree well with their estimate, and a comparison of Δ_π is shown in Fig. 15.

Our 5-GeV/c Δ_K agrees fairly well with the final[7] (but not the preliminary[6]) results of Chabaud *et al.* Our data extend to smaller t, while Chabaud *et al.* have better statistics at large t. Some small systematic differences can be seen in Fig. 16.

TABLE XVIII. Results of fitting Δ [Eq. (27)] over the $-t$ range 0–0.8 GeV^2 to the form $ae^{bt}J_0(r(-t)^{1/2})$.

Beam	p_{beam} (GeV/c)	a [(mb/GeV^2)$^{1/2}$]	b (GeV^{-2})	r (GeV^{-1})	χ^2 per degree of freedom
π	3	0.19 ± 0.06	0.16 ± 0.92	6.39 ± 0.34	13/9
	3.65	0.19 ± 0.05	−0.44 ± 0.66	5.75 ± 0.28	3/8
	5	0.16 ± 0.04	−0.20 ± 0.66	5.91 ± 0.25	12/8
	6	0.10 ± 0.04	−1.23 ± 0.97	6.31 ± 0.20	5/8
K	3	0.88 ± 0.04	−0.18 ± 0.11	5.46 ± 0.05	52/28
	3.65	0.81 ± 0.04	0.15 ± 0.12	5.31 ± 0.07	43/27
	5	0.65 ± 0.04	0.24 ± 0.13	5.40 ± 0.07	34/27
	6	0.60 ± 0.04	0.40 ± 0.15	5.28 ± 0.08	21/26
p	3	3.34 ± 0.09	1.28 ± 0.09	6.13 ± 0.05	44/28
	3.65	2.95 ± 0.10	1.16 ± 0.11	6.10 ± 0.05	18/27
	5	2.24 ± 0.10	1.00 ± 0.13	6.10 ± 0.06	15/27
	6	1.97 ± 0.12	0.89 ± 0.16	5.88 ± 0.09	28/26

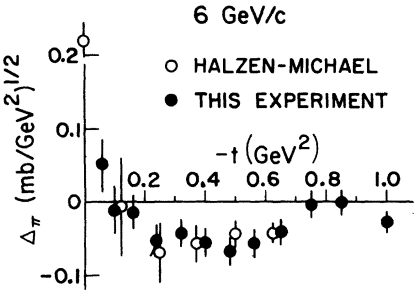

FIG. 15. Comparison of Δ_π from this experiment with the compilation by Halzen and Michael (Ref. 2).

The energy dependence of Δ has been studied using the form

$$\Delta = cs^{\alpha-1} \tag{29}$$

with separate fits at each t to data from all four energies. The parameter c is a constant and α is the effective Regge trajectory. If ω or ρ exchange is important, one expects

$$\alpha \approx 0.5 + t\,. \tag{30}$$

The fitted results for α are compared in Fig. 17 with the expected trajectory. The pion error bars are too large for any conclusion to be drawn. The kaon points lie along the expected line, although with large fluctuations. The proton α is close to zero for $0 \leq -t < 0.4$ GeV^2, after which it increases, suggesting that other exchanges or cuts are important, or that the dominant amplitude is no longer imaginary nonflip.

K. ω and ρ universality

SU(3) symmetry with F-type coupling, as given by the quark-model predictions of Barger *et al.*, suggests[61]

$$\Delta_p = 3\Delta_K\,, \tag{31}$$

$$\Delta_K = \tfrac{3}{2}\Delta_\pi\,. \tag{32}$$

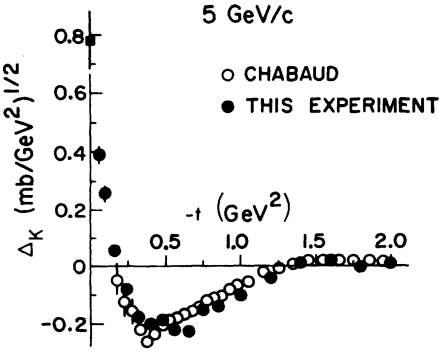

FIG. 16. Comparison of Δ_K from this experiment with the final results of Chabaud *et al.* (Ref. 7).

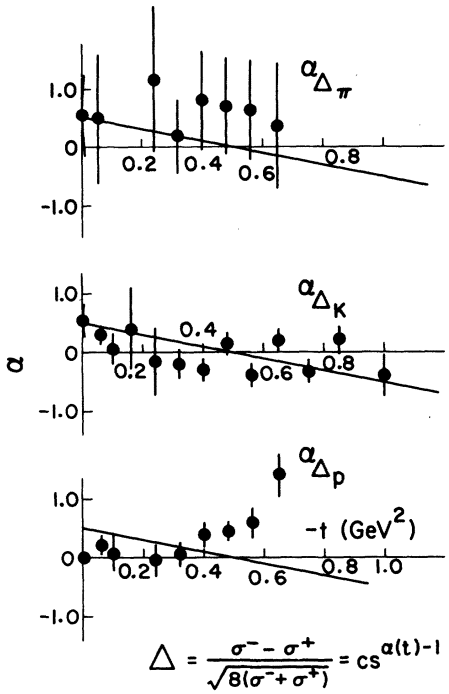

FIG. 17. Comparison of the effective trajectory for the Δ's found in this experiment with the expected ρ, ω Regge trajectory, $\alpha(t) = 0.5 + t$. At each t the four values of Δ were fitted to the form shown.

Figure 18 compares Δ_p and $3\Delta_K$; the ω-universality prediction of Eq. (31) agrees with the data qualitatively, the agreement becoming better as the energy increases. Among other things, the difference in kaon and proton crossover points precludes quantitative agreement. Nucleon form fac-

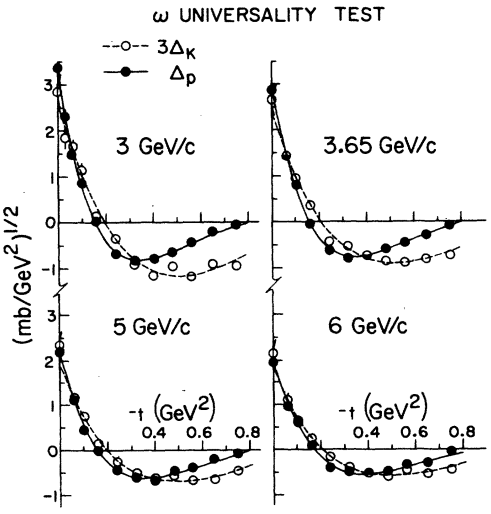

FIG. 18. Comparison of the results from this experiment with the ω-universality prediction, $\Delta_p = 3\Delta_K$.

tor information indicates that Eq. (32) may not be reliable. Indeed, it is badly broken as shown in Fig. 19; at 6 GeV/c $\frac{3}{2}\Delta_\pi$ is typically a factor of 2 or 3 smaller than Δ_K.

V. πN AMPLITUDE ANALYSIS

Model-independent determinations of πN scattering amplitudes have been carried out by Halzen and Michael[2] and others[3-5] at 6 GeV/c. Since the elastic-cross-section differences are a sensitive ingredient in these calculations, we have done a t-independent analysis using the cross sections of this experiment and also taking into account recent Argonne charge-exchange (CEX) polarization measurements.[65]

Numerically our results are consistent with previous determinations; as expected, the new cross-section measurements reduce the uncertainties in the $I_t=1$ amplitudes. The general agreement is not surprising since there is a large overlap of the input data with that used in previous analyses. Although Halzen and Michael[2] had to average and interpolate the elastic-scattering data available at the time, the comparison with the cross-section differences of this experiment (Fig. 15) shows agreement well within the error bars. The polarization and spin rotation parameter data are the same in all analyses, except that there is considerable spread in the measurements of P^0, the CEX polarization, affecting mainly the real nonflip amplitude for $I_t=1$. Depending on whether P^0 is small (20%) (Ref. 65) or large (40%) (Ref. 66), this amplitude has a crossover zero at $-t=0.25$ GeV^2 or remains positive out to $-t\simeq 0.5$ GeV^2.

The analyses do differ for $-t>0.5$ GeV^2, where spin rotation data are not available. Attempts to "determine" the amplitudes in this region, either by extrapolating the R parameters or by extrapolating the amplitudes (t-dependent analysis), may or may not be correct. Clearly the structure of the amplitudes beyond $-t=0.6$ GeV^2 deserves careful investigation (R and A measurements) and cannot be decided solely by extrapolation procedures. The only model-independent analysis presently possible for $-t\gtrsim 0.6$ GeV^2 must use the limit $R^2\leq 1-P^2$.

A. Definitions and data set

We use the same notation as Halzen and Michael;[2] namely, F^I_{++} (F^I_{+-}) denotes the s-channel helicity-nonflip (flip) amplitude having isospin $I_t=0$ or 1 in the t channel. Since the over-all phase is arbitrary, we measure phases relative to F^0_{++}, which is empirically the dominant amplitude. $(F)_\parallel$ and $(F)_\perp$ denote amplitude components in the complex plane along F^0_{++} and orthogonal to F^0_{++}, respectively. The isospin decomposition is given by

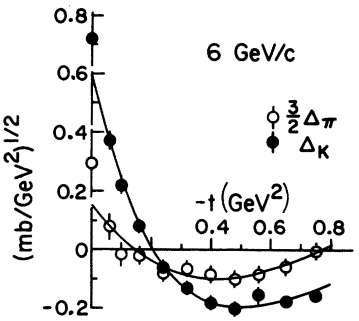

FIG. 19. Comparison of the results from this experiment with the quark-model prediction for ρ universality, $\Delta_K=\frac{3}{2}\Delta_\pi$.

$$F(\pi^\pm p\to\pi^\pm p)=F^0\mp F^1,$$
$$F(\pi^- p\to\pi^0 n)=\sqrt{2}\,F^1. \tag{33}$$

The observables are given by

$$\frac{d\sigma}{dt}=|F_{++}|^2+|F_{+-}|^2, \tag{34}$$

$$-P\frac{d\sigma}{dt}=2\,\mathrm{Im}(F_{++}F^*_{+-}), \tag{35}$$

$$-R\frac{d\sigma}{dt}=(|F_{++}|^2-|F_{+-}|^2)\cos\theta_R + 2\,\mathrm{Re}(F_{++}F^*_{+-})\sin\theta_R, \tag{36}$$

$$A\frac{d\sigma}{dt}=(|F_{++}|^2-|F_{+-}|^2)\sin\theta_R - 2\,\mathrm{Re}(F_{++}F^*_{+-})\cos\theta_R, \tag{37}$$

where θ_R denotes the laboratory angle of the recoil proton.

The data used in the present analysis are taken from this experiment and Refs. 65 and 67–73. Within each t bin (of width 0.1 GeV^2) values of $\ln(d\sigma^\pm/dt)$ and $(-t)^{-1/2}P^\pm$ were interpolated linearly; the CEX cross section was assumed to scale as $1/s$ and $\ln(d\sigma^0/dt)$ was interpolated quadratically in t. The quantities $(-t)^{-1/2}P^0$ (at 5 GeV/c) and $(-t)^{-1/2}R^\pm$ were fitted to third-order polynomials over the entire interval $0\leq -t<0.6$ GeV^2. For $-t>0.6$ GeV^2 the possible range of solutions was determined by setting $R=0\pm(1-P^2)^{1/2}$. The interpolated data are listed in Table XIX.

B. Ambiguities

In general, quadratic ambiguities arise from the possibility of changing various signs or interchanging F_{++} and F_{+-}. These ambiguities are resolved at $t=0$, where $F_{+-}=0$ and where the phases of F^0_{++} and F^1_{++} are known from dispersion

TABLE XIX. Input data used for πN amplitude analysis at 6 GeV/c.

$-t$ (GeV^2)	$d\sigma^-/dt$ (mb/GeV^2)	$d\sigma^+/dt$ (mb/GeV^2)	$d\sigma^0/dt$ (mb/GeV^2)	P^-	P^+	P^0	R^-	R^+
0.0	41.57 ± 1.00	36.67 ± 1.40	0.362 ± 0.070	0	0	0	0	0
0.05	27.61 ± 0.29	26.09 ± 0.38	0.423 ± 0.030	−0.15 ± 0.02	0.20 ± 0.05	0.13 ± 0.02	−0.02 ± 0.21	0.14 ± 0.20
0.15	12.64 ± 0.15	12.90 ± 0.19	0.266 ± 0.019	−0.137 ± 0.005	0.205 ± 0.007	0.18 ± 0.02	−0.13 ± 0.15	0.05 ± 0.14
0.25	5.723 ± 0.100	6.262 ± 0.133	0.110 ± 0.012	−0.116 ± 0.006	0.185 ± 0.006	0.18 ± 0.03	−0.22 ± 0.08	−0.06 ± 0.06
0.35	2.789 ± 0.072	3.119 ± 0.094	0.038 ± 0.004	−0.071 ± 0.008	0.161 ± 0.007	0.15 ± 0.04	−0.25 ± 0.06	−0.11 ± 0.05
0.45	1.261 ± 0.062	1.515 ± 0.084	0.013 ± 0.002	−0.016 ± 0.011	0.122 ± 0.011	0.12 ± 0.04	−0.23 ± 0.09	−0.07 ± 0.07
0.55	0.631 ± 0.034	0.834 ± 0.048	0.0059 ± 0.0011	0.038 ± 0.019	0.090 ± 0.014	0.07 ± 0.04	−0.15 ± 0.20	0.03 ± 0.18
0.65	0.376 ± 0.027	0.480 ± 0.038	0.0059 ± 0.0011	0.010 ± 0.023	0.024 ± 0.018	0.04 ± 0.05	0 ± 1	0 ± 1
0.80	0.199 ± 0.015	0.202 ± 0.018	0.0082 ± 0.0009	−0.067 ± 0.039	0.090 ± 0.036	0 ± 0.05	0 ± 1	0 ± 1

relations and Coulomb interference measurements. Also, the solutions are unique so far as the F^0 amplitudes are concerned; $(F^0_{++})_\parallel$ is so much larger than any other amplitude in the t region of interest that it is impossible to change smoothly to another solution with, for example, $(F^0_{++})_\parallel$ and $(F^0_{+-})_\parallel$ interchanged.

To get a feeling for the possible ambiguities, consider the case where $(F^0_{++})_\parallel$ is dominant; then

$$(F^0_{++})_\parallel \approx [\tfrac{1}{2}(\sigma^- + \sigma^+)]^{1/2}. \tag{38}$$

The remaining amplitudes [except for $(F^1_{++})_\perp$] can be found from their interference with $(F^0_{++})_\parallel$:

$$4(F^0_{++})_\parallel (F^1_{++})_\parallel \approx \sigma^- - \sigma^+, \tag{39}$$

$$-4(F^0_{++})_\parallel (F^0_{+-})_\parallel \approx \frac{(R^- + \cos\theta_R)\sigma^- + (R^+ + \cos\theta_R)\sigma^+}{\sin\theta_R}, \tag{40}$$

$$-4(F^0_{++})_\parallel (F^1_{+-})_\parallel \approx (R^-\sigma^- - R^+\sigma^+)/\sin\theta_R, \tag{41}$$

$$-4(F^0_{++})_\parallel (F^0_{+-})_\perp \approx P^-\sigma^- + P^+\sigma^+, \tag{42}$$

$$-4(F^0_{++})_\parallel (F^1_{+-})_\perp \approx P^-\sigma^- - P^+\sigma^+. \tag{43}$$

Unfortunately the R-parameter difference is not accurate enough to determine much more than the sign of $(F^1_{+-})_\parallel$, and in practice $(F^1_{+-})_\parallel$ and $(F^1_{++})_\perp$ are fixed by the quadratic relations

$$(F^1_{++})_\perp{}^2 + (F^1_{+-})_\parallel{}^2 = \tfrac{1}{2}\sigma^0 - (F^1_{++})_\parallel{}^2 - (F^1_{+-})_\perp{}^2, \tag{44}$$

$$2(F^1_{++})_\perp (F^1_{+-})_\parallel = \tfrac{1}{2}P^0\sigma^0 + 2(F^1_{++})_\parallel (F^1_{+-})_\perp. \tag{45}$$

The amplitudes $(F^1_{++})_\parallel$ and $(F^1_{+-})_\perp$ appearing on the right-hand side of Eqs. (44) and (45) are determined by the cross-section and polarization differences [Eqs. (39) and (43)]. Note that in Eq. (45) the product $(F^1_{++})_\parallel (F^1_{+-})_\perp$ is often larger than $\frac{1}{4}P^0\sigma^0$, and the cross-section difference which gives $(F^1_{++})_\parallel$ is a major source of uncertainty in the solution of Eqs. (44) and (45).

Given one solution for Eqs. (44) and (45), we can immediately generate three more solutions by changing the signs of both $(F^1_{++})_\perp$ and $(F^1_{+-})_\parallel$, or interchanging $(F^1_{++})_\perp$ and $(F^1_{+-})_\parallel$, or both. At $t=0$ the solution is unique [$(F^1_{++})_\perp > 0$, $(F^1_{+-})_\parallel = 0$], but away from $t=0$ continuity can determine the correct solution only so long as two solutions do not cross. Continuity thus fails when $(F^1_{++})_\perp \approx \pm(F^1_{+-})_\parallel$; experimentally this happens at both $-t \simeq 0.05$ and at $-t \simeq 0.4$ GeV^2. Between 0.05 and 0.5 GeV^2 the R-parameter differences are needed to resolve the resulting ambiguity via Eq. (41). The preferred solution has a large positive $(F^1_{+-})_\parallel$ and a small $(F^1_{++})_\perp$. There are no R-parameter measurements for large t, and the errors were calculated with $R = 0 \pm (1 - P^2)^{1/2}$ for $-t \geq 0.6$ GeV^2.

The ambiguity conditions $(F^1_{++})_\perp \pm (F^1_{+-})_\parallel$ are closely related to isospin bounds.[74] The isospin triangle becomes degenerate and the isospin bounds saturate when the $I_t = 0$ and $I_t = 1$ amplitudes are parallel in the complex plane. A particularly useful set of amplitudes in this regard is discussed by Höhler *et al.*[75]: $F^1_{++} \pm iF^1_{+-}$ and $F^0_{++} \pm iF^0_{+-}$. When these vectors are parallel in the complex plane

$$\frac{(F^1_{++})_\perp \mp (F^1_{+-})_\parallel}{(F^1_{++})_\parallel \pm (F^1_{+-})_\perp} = \frac{0 \mp (F^0_{+-})_\parallel}{(F^0_{++})_\parallel \pm (F^0_{+-})_\perp}. \tag{46}$$

The right-hand side is very small [due to the large term $(F^0_{++})_\parallel$ in the denominator] and the isospin bound is saturated for $(F^1_{++})_\perp \approx \pm(F^1_{+-})_\parallel$, the ambiguity condition.

In the actual analysis, the approximations of Eqs. (38)–(43) were not used, but rather exact solutions to the basic Eqs. (34)–(37) were found, ignoring the R^+ measurement (the procedure originally used by Halzen and Michael). Then each solution was pulled to minimize the over-all χ^2 with the R^+ data included.

The error matrix proved to be nearly singular at $-t = 0.05$ GeV^2, where $(F^1_{++})_\perp \approx (F^1_{+-})_\parallel$. The reason for this can be understood as follows: If we "fitted" $(F^1_{++})_\perp$ and $(F^1_{+-})_\parallel$ alone using Eqs. (44) and (45), the resulting error matrix would be ex-

actly singular when $(F^1_{++})_\perp = (F^1_{+-})_\parallel$. To avoid this difficulty, we estimated errors using Monte Carlo techniques. Data sets were generated corresponding to Gaussian errors on the experimental data; a data set was rejected if it did not satisfy isospin bounds. The amplitude errors were then defined to be the mean square spread in the Monte Carlo results. This procedure agreed with the original error matrix determination in those regions where the isospin bounds were not saturated.

C. Amplitude results

The results of the amplitude analysis are listed in Table XX. The F^0 amplitudes, shown in Fig. 20, approximately conserve s-channel helicity, although the deviation is typically 10%. It is noteworthy that F^0_{+-} is nearly in phase with F^0_{++}. Exchange of the f trajectory could be the source of the helicity-flip amplitude, but this seems not to be the case. In a Regge picture f-exchange amplitudes should be rotated about 45° with respect to Pomeron exchange, in which case we would expect $(F^0_{+-})_\perp \approx -(F^0_{+-})_\parallel$, contrary to the results in Fig. 20. The observed energy dependence of R^- is also consistent with F^0_{+-} being mainly associated with Pomeron exchange.[4]

The amplitude $(F^1_{++})_\parallel$ shown in Fig. 21(a) has the expected crossover zero at $-t \approx 0.15$ GeV^2. The amplitude $(F^1_{++})_\perp$ has a zero at $-t \approx 0.25$ GeV^2. However, if the CEX polarization of Ref. 66 is used ($P^0 \approx 40\%$ instead of 20%), $(F^1_{++})_\perp$ is increased by 0.07 (mb/GeV^2)$^{1/2}$ and remains positive everywhere.

The ambiguity condition $(F^1_{++})_\perp \approx -(F^1_{+-})_\parallel$ occurs near $-t = 0.4$ GeV^2. At larger t the two solutions [with $(F^1_{++})_\perp$ and $-(F^1_{+-})_\parallel$ interchanged] are shown in Fig. 21.

Since absorptive corrections should be relatively small for helicity-flip amplitudes at small t,[62] F^1_{+-} is expected to exhibit Regge-pole behavior in this region; this amplitude is shown in Fig. 21(b). It has the remarkable property that $(F^1_{+-})_\parallel/(F^1_{+-})_\perp \simeq 0.6$ out to $-t = 0.4$ GeV^2, with the phase difference between F^1_{+-} and F^0_{++} [Fig. 21(c)] approximately constant:

$$\phi^0_{++} - \phi^1_{+-} \approx 60^\circ . \tag{47}$$

Assuming pure ρ exchange, F^1_{+-} rotates counterclockwise with increasing t:

$$\phi^1_{+-}(\rho) = \tfrac{1}{2}\pi[1 - \alpha_\rho(t)] \simeq 40^\circ + 90^\circ |t| \tag{48}$$

for t in GeV^2. Equations (47) and (48) are consistent at $t = 0$, where dispersion relations give $\phi^0_{++} = 101^\circ$.[31] If F^1_{+-} does in fact rotate in this manner, then the constant relative phase between the two amplitudes implies that F^0_{++} must also rotate,

$$\phi^0_{++} \simeq 101^\circ + 90^\circ |t| , \tag{49}$$

in which case the slope of the Pomeron trajectory would be similar to that of the ρ. This result agrees with forward derivative-dispersion calculations which indicate that F^0_{++} rotates counterclockwise at small t.[76]

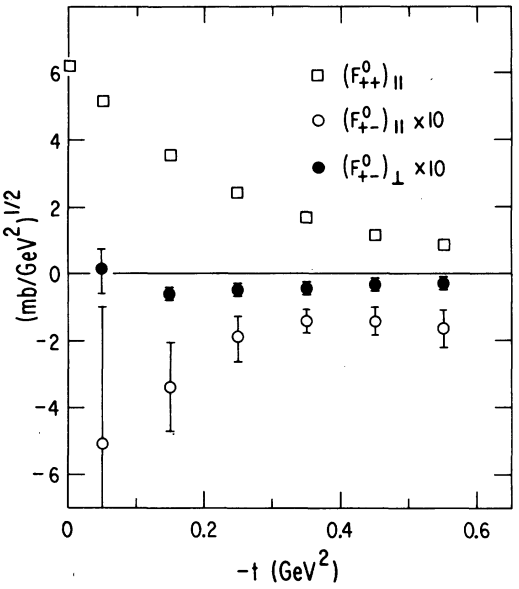

FIG. 20. S-channel helicity amplitudes for πN scattering at 6 GeV/c with $I_t = 0$. The amplitude $(F^0_{++})_\perp$ is defined to be zero.

TABLE XX. πN amplitudes at 6 GeV/c in (mb/GeV^2)$^{1/2}$.

$-t$ (GeV^2)	F^0_{++}	$(F^0_{+-})_\parallel$	$(F^0_{+-})_\perp$	$(F^1_{++})_\parallel$	$(F^1_{++})_\perp$	$(F^1_{+-})_\parallel$	$(F^1_{+-})_\perp$
0.0	6.24 ± 0.080	0	0	0.20 ± 0.06	0.38 ± 0.08	0	0
0.05	5.14 ± 0.060	−0.51 ± 0.41	0.02 ± 0.08	0.085 ± 0.028	0.196 ± 0.077	0.22 ± 0.11	0.345 ± 0.062
0.15	3.54 ± 0.023	−0.34 ± 0.14	−0.061 ± 0.009	0.005 ± 0.024	0.071 ± 0.048	0.190 ± 0.029	0.303 ± 0.011
0.25	2.43 ± 0.014	−0.19 ± 0.07	−0.049 ± 0.006	−0.044 ± 0.020	−0.029 ± 0.031	0.123 ± 0.026	0.189 ± 0.007
0.35	1.71 ± 0.014	−0.15 ± 0.03	−0.044 ± 0.005	−0.041 ± 0.018	−0.044 ± 0.034	0.065 ± 0.031	0.106 ± 0.006
0.45	1.16 ± 0.022	−0.15 ± 0.04	−0.035 ± 0.005	−0.036 ± 0.026	−0.026 ± 0.024	0.048 ± 0.016	0.046 ± 0.007
0.55	0.834 ± 0.023	−0.16 ± 0.05	−0.030 ± 0.005	−0.036 ± 0.021	−0.015 ± 0.025	0.03 ± 0.02	0.015 ± 0.007

The amplitude $(F^1_{+-})_\perp$ can be calculated using Eq. (43); this approximation compares well with our amplitude analysis result at 6 GeV/c. Using polarization and cross-section data from 2.8 to 14 GeV/c incident momentum,[43,77-81] we found the energy dependence of $(F^1_{+-})_\perp$ in terms of the effective trajectory, as shown in Fig. 22. For $-t>0.1$ GeV^2, $(F^1_{+-})_\perp$ falls faster than expected from the ρ trajectory $\alpha_\rho = 0.55 + t$, found from the CEX cross section,[82] $\sigma^0 \approx |F^1_{+-}|^2$. Although it is possible that $(F^1_{+-})_\perp$ and $(F^1_{+-})_\parallel$ have different energy dependences, the Regge description of F^1_{+-} could still be valid if the anomalous energy dependence of $(F^1_{+-})_\perp$ were ascribed to a substantial f-exchange contribution to F^0_{++}. At fixed t, F^0_{++} would then rotate clockwise as s increased and the f contribution diminished relative to the Pomeron. $(F^1_{+-})_\perp$ would then be measured relative to a rotating axis and, as s increased, the projection $(F^1_{+-})_\perp$ would fall faster than otherwise expected.[83] The explanations of the behavior shown in Fig. 22 would require an f-exchange contribution to F^0_{++} of about 30% and would favor a smaller slope for the Pomeron trajectory.

Thus, one consistent picture of the amplitudes would be that while F^1_{++} suffers large absorptive corrections, both F^0_{++} and F^1_{+-} are approximately Regge-behaved, with phases rotating counterclockwise with t; there would be a large f contribution to F^0_{++} at low energies, but the helicity-nonconserving amplitude F^0_{+-} would be associated mainly with Pomeron exchange.

VI. CONCLUSIONS

Approximately 300 000 elastic scattering events have been used to measure differential cross sections for six different beam particles scattering from protons. A total of 930 differential cross sections are tabulated in Table VIII for $0.02 < -t < 2$ GeV^2 and incident momenta 3, 3.65, 5, and 6 GeV/c.

Strong elastic scattering signals with little background were found in the missing-mass distributions (Fig. 2) calculated from the angle and momentum of the fast scattered particle. The overall uncertainty in absolute normalization is estimated to be ±4%, with an uncertainty in particle-antiparticle relative normalization of ±1.5% (Table IV).

The $\pi^\pm$ and $K^\pm$ data fit well to straight lines out to about 0.5 GeV^2 on the semilog plot of $\ln(d\sigma/dt)$ vs t (Fig. 3). Both the proton and antiproton data show curvature on the semilog plot and were fitted to quadratics in t. Extrapolated to $t=0$, the fits generally agree well with the predictions of the

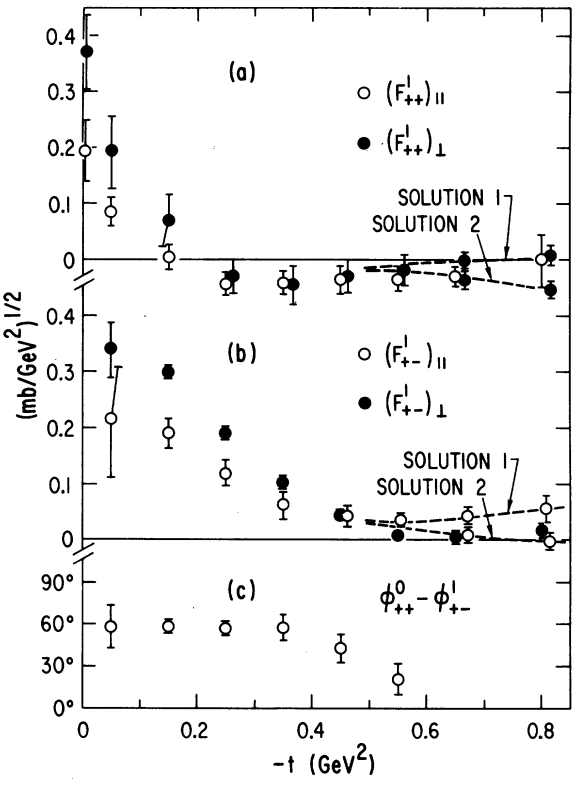

FIG. 21. (a) S-channel helicity-nonflip amplitudes found for $I_t = 1$. (b) Helicity-flip amplitudes. At large t the ambiguity between the two solutions with $(F^1_{++})_\perp$ and $-(F^1_{+-})_\parallel$ interchanged cannot be resolved without spin rotation information. (c) Relative phase between F^0_{++} and F^1_{+-}.

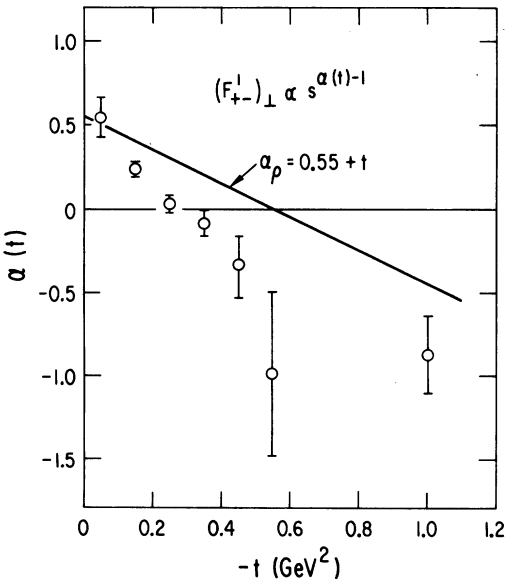

FIG. 22. Energy dependence of $(F^1_{+-})_\perp$ in terms of an effective trajectory, $\alpha(t)$. The nominal ρ trajectory $\alpha_\rho(t) = 0.55 + t$ is shown for comparison.

optical theorem corrected for the real-to-imaginary ratio (Fig. 4). The results of this experiment are in reasonable agreement with those of previous experiments (Fig. 5), the spread in previous results precluding good agreement everywhere.

Only the proton and K^+ forward slopes show shrinkage in our data (Fig. 7), the $\pi^\pm$ and $\bar{p}$ slopes being constant within one standard deviation and the K^- data showing marginal antishrinkage (1.7 standard deviations). The slopes found when plotting the data vs the Leader-Pennington[48] variable n^2 all show substantial energy dependence. Although our forward slopes agree qualitatively with the geometric model of Krisch,[49] the K^- radius obtained in that model is energy-dependent and differs from the K^+ radius (Fig. 9).

The crossover points for all three particles are independent of momentum from 3 to 6 GeV/c to within one standard deviation (Fig. 13). The average values are 0.14 ± 0.03 0.190 ± 0.006, and 0.162 ± 0.004 GeV^2 for π, K, and proton, respectively. Equating the first zero of $J_0(r(-t)^{1/2})$ with the crossover point, these average values correspond to interaction radii of 1.27 ± 0.13, 1.09 ± 0.02, and 1.18 ± 0.02 F. While the momentum independence of crossover position is expected in simple geometric models, it does disagree with several other models.[49,57-60]

To a good approximation, the quantity Δ [Eq. (27)] should represent that part of the $C=-1$ amplitude in phase (both in the complex plane and in spin space) with the dominant Pomeron-exchange amplitude. The experimental values found for Δ in the region $0 \leq -t < 0.8$ GeV^2 gave reasonable fits to the form $ae^{bt}J_0(r(-t)^{1/2})$ suggested by Davier and Harari[1] on the basis of the dual absorption model (Fig. 14). At larger t, however, Δ approaches zero gradually rather than passing through the second crossover zero of the Bessel function.

The energy dependence of Δ_K is roughly that expected from the ω trajectory (Fig. 17). However, the effective trajectory derived from the Δ_p energy dependence is close to zero for $0 \leq -t < 0.4$ GeV^2, after which it increases, suggesting that at these energies contributions other than ω exchange are important.

The ω-universality prediction[61] $\Delta_p = 3\Delta_K$ is in qualitative agreement with the data (Fig. 18), the agreement improving with increasing momentum. Among other things, the difference in kaon and proton crossover position precludes quantitative agreement. The corresponding ρ-universality prediction $\Delta_K = \frac{3}{2}\Delta_\pi$ is badly violated (Fig. 19).

The results of a t-independent amplitude analysis are shown in Figs. 20 and 21 for πN scattering at 6 GeV/c. For $I_t = 0$, the s-channel helicity-flip amplitude is typically 10% of the nonflip amplitude and the two amplitudes are nearly in phase with one another. The relative phase between the $I_t = 0$ nonflip amplitude and the $I_t = 1$ flip amplitude remains approximately constant at 60° and suggests that the effective trajectories of the two amplitudes (presumably dominated by Pomeron and ρ exchange, respectively) have equal slopes.

ACKNOWLEDGMENTS

We would like to thank Dr. T. Fields for suggesting this experiment, R. Diaz, J. Falout, L. Filips, and E. Walschon for help in the design, construction, and operation of the apparatus, and R. Ely and C. Klindworth for assistance with the on-line computer system. We are indebted to Dr. R. Klem, R. Giugler, A. Passi, W. Siljander, and the other members of the High Energy Facilities Division for their help with the building and operation of the beam, Čerenkov counters, and hydrogen target. The Accelerator Division personnel provided the stable, reproducible beam required for this experiment. We particularly thank Dr. B. Cork and Dr. T. Fields for support and encouragement during all phases of this work.

---

*Work performed under the auspices of the U. S. Atomic Energy Commission.

†Present address: National Accelerator Laboratory, Batavia, Illinois 60510.

‡Present address: Ohio State University, Columbus, Ohio 43210.

§Present address: Indiana University, Bloomington, Indiana 47401.

[1] M. Davier and H. Harari, Phys. Lett. 35B, 239 (1971).
[2] F. Halzen and C. Michael, Phys. Lett. 36B, 367 (1971).
[3] R. L. Kelly, Phys. Lett. 39B, 635 (1972).
[4] G. Cozzika *et al.*, Phys. Lett. 40B, 281 (1972).
[5] P. Johnson *et al.*, Phys. Rev. Lett. 30, 242 (1973).
[6] V. Chabaud *et al.*, Phys. Lett. 38B, 441 (1972).
[7] V. Chabaud *et al.*, CERN NP Internal Report No. 72-12, 1972 (unpublished).
[8] D. R. Rust *et al.*, Phys. Rev. Lett. 24, 1361 (1970).
[9] C. T. Coffin *et al.*, Phys. Rev. 159, 1169 (1967).
[10] J. N. MacNaughton *et al.*, Nucl. Phys. B14, 237 (1969).
[11] W. DeBaere *et al.*, Nuovo Cimento 45A, 885 (1966).
[12] C. W. Akerlof *et al.*, Phys. Rev. Lett. 26, 1278 (1971).
[13] M. Aguilar-Benitez, R. L. Eisner, and J.B. Kinson, Phys. Rev. D 4, 2583 (1971).
[14] J. Mott *et al.*, Phys. Lett. 23, 171 (1966).

[15]D. P. Owen *et al.*, Phys. Rev. 181, 1794 (1969).
[16]A. R. Clyde, thesis, LBL Report No. UCRL 16275, 1966 (unpublished).
[17]K. Böckmann *et al.*, Nuovo Cimento 42A, 954 (1966).
[18]R. Engelmann *et al.*, Phys. Rev. D 5, 2162 (1972).
[19]A. Seidl, Phys. Rev. D 7, 621 (1973).
[20]B. Escoubès *et al.*, Phys. Lett. 5, 132 (1963).
[21]O. Czyzewski *et al.*, Phys. Lett. 15, 188 (1965).
[22]Howard A. Gordon, Kwan-Wu Lai, and Frank E. Paige, Phys. Rev. D 5, 1113 (1972).
[23]R. Diebold, in *Proceedings of the XVI International Conference on High Energy Physics, Chicago-Batavia, Ill., 1972*, edited by J. D. Jackson and A. Roberts (NAL, Batavia, Ill., 1973), Vol. 2, p. 447; D. S. Ayres, in *Proceedings of the 1973 International Conference on Instrumentation for High Energy Physics, Frascati, Italy*, edited by Stanislao Stipcich, (Laboratori Nazionali del C.N.E.N. Servizio Documentazione, Frascati, Italy, 1973), p. 665.
[24]I. Ambats *et al.*, Phys. Rev. Lett. 29, 1415 (1972).
[25]A. B. Wicklund, E. C. Berrill, and T. W. Hardek, Argonne Technical Note, 1971 (unpublished).
[26]D. D. Briggs, D. S. Ayres, and E. Walschon, Nucl. Instrum. Methods 95, 377 (1971).
[27]C. E. W. Ward, ANL Report No. ANL/HEP 7206, 1972 (unpublished).
[28]R. J. Tapper, Rutherford Report No. NIRL/R/95, 1965 (unpublished).
[29]Michael R. Sogard, this issue, Phys. Rev. D 9, 1486 (1974).
[30]K. J. Foley *et al.*, Phys. Rev. 181, 1775 (1969).
[31]G. Höhler and R. Strauss, University of Karlsruhe report, 1971 (unpublished).
[32]M. Lusignoli, M. Restignoli, G. Violini, and G. A. Snow, Nuovo Cimento 45A, 792 (1966).
[33]T. H. J. Bellm *et al.*, Phys. Lett. 33B, 438 (1970).
[34]G. Giacomelli, CERN Report No. CERN/HERA 69-3, 1969 (unpublished).
[35]P. Söding, Phys. Lett. 8, 285 (1964).
[36]Geoffrey B. West and D. R. Yennie, Phys. Rev. 172, 1413 (1968).
[37]G. Höhler and H. M. Staudenmaier, University of Karlsruhe report, 1972 (unpublished).
[38]P. H. Eberhard, Nucl. Phys. B48, 333 (1972).
[39]A. D. Martin and F. Poole, Nucl. Phys. B4, 467 (1968).
[40]R. Henzi, A. Kotański, D. Morgan, and L. Van Hove, Nucl. Phys. B16, 1 (1970).
[41]Previous results for the total elastic scattering cross sections were taken from the CERN/HERA compilations 70-2, 72-1, and 72-2 (unpublished) and the Particle Data Group compilation LBL Report No. LBL-58, 1972 (unpublished).
[42]T. Lasinski, R. Levi Setti, B. Schwarzschild, and P. Ukleja, Nucl. Phys. B37, 1 (1972).
[43]K. J. Foley *et al.*, Phys. Rev. Lett. 11, 425 (1963).
[44]E. Krubasik, Nucl. Phys. B44, 558 (1972).
[45]B. A. Ryan *et al.*, Phys. Rev. D 3, 1 (1971).
[46]G. Alexander *et al.*, Phys. Rev. 173, 1322 (1968).
[47]D. Harting *et al.*, Nuovo Cimento 38, 60 (1965).
[48]E. Leader and M. R. Pennington, Phys. Rev. Lett. 27, 1325 (1971).
[49]A. D. Krisch, Phys. Lett. 44, 71 (1973).
[50]G. Barbiellini *et al.*, Phys. Lett. 39B, 663 (1972).
[51]R. A. Carrigan, Jr., Phys. Rev. Lett. 24, 168 (1970).
[52]M. Davier, Phys. Lett. 40B, 369 (1972).
[53]V. Barger, K. Geer, and F. Halzen, Nucl. Phys. B49, 302 (1972).
[54]G. V. Dass, C. Michael, and R. J. N. Phillips, Nucl. Phys. B9, 549 (1969).
[55]R. K. Carnegie *et al.*, contribution to the XVI International Conference on High Energy Physics, Chicago-Batavia, Ill., 1972 (unpublished).
[56]C. Michael, in *Proceedings of the Fourth International Conference on High Energy Collisions, Oxford, 1972*, edited by J. R. Smith (Rutherford High Energy Laboratory, Chilton, Didcot, Berkshire, England, 1972), Vol. 1, p. 415.
[57]D. Cline and J. Matos, Nucl. Phys. B33, 421 (1971).
[58]B. J. Hartley and G. L. Kane, Phys. Lett. 39B, 531 (1972).
[59]Robert T. Park, N. Barik, and David T. Gregorich, Phys. Rev. D 6, 3162 (1972).
[60]R. Henzi, A. Mackay, B. Margolis, and W. A. Ross, Phys. Rev. D 5, 2754 (1972).
[61]V. Barger, K. Geer, and F. Halzen, Nucl. Phys. B44, 475 (1972).
[62]M. Ross, F. S. Henyey, and G. L. Kane, Nucl. Phys. B23, 269 (1970)
[63]G. Höhler and H. M. Staudenmaier, University of Karlsruhe report, 1972 (unpublished).
[64]N. Masuda, Phys. Rev. D 7, 1474 (1973).
[65]D. Hill *et al.*, Phys. Rev. Lett. 30, 239 (1973).
[66]P. Bonamy *et al.*, Nucl. Phys. B52, 392 (1973).
[67]M. Borghini *et al.*, Phys. Lett. 31B, 405 (1970).
[68]D. D. Drobnis *et al.*, Phys. Rev. Lett. 20, 274 (1968).
[69]P. Bonamy *et al.*, Nucl. Phys. B16, 335 (1970).
[70]A. V. Stirling *et al.*, Phys. Rev. Lett. 14, 763 (1965).
[71]P. Sonderegger *et al.* Phys. Lett. 20, 75 (1966).
[72]M. A. Wahlig and I. Mannelli, Phys. Rev. 168, 1515 (1968).
[73]A. de Lesquen *et al.*, Phys. Lett. 40B, 277 (1972).
[74]G. V. Dass *et al.*, Phys. Lett. 36B, 339 (1971).
[75]G. Höhler *et al.*, Nuovo Cimento Lett. 5, 413 (1972).
[76]G. Höhler and H. P. Jakob, Nuovo Cimento Lett. 2, 485 (1971).
[77]R. J. Esterling *et al.*, Phys. Rev. Lett. 21, 1410 (1968).
[78]M. Borghini *et al.*, Phys. Lett. 36B, 493 (1971).
[79]M. Borghini *et al.*, CERN report, 1972 (unpublished) [corrections to Phys. Lett. 36B, 493 (1971)].
[80]M. G. Albrow *et al.*, Nucl. Phys. B25, 9 (1970).
[81]M. G. Albrow *et al.*, Nucl. Phys. B37, 594 (1972).
[82]V. Barger and R. J. N. Phillips, Phys. Rev. 187, 2210 (1969).
[83]G. Ringland (private communication).